Vibration modes and wave propagation of the rail under fastening constraint

Zhang, Pan; Li, Shaoguang; Núñez, Alfredo; Li, Zili

DOI
10.1016/j.ymssp.2021.107933

Publication date
2021

Document Version
Final published version

Published in
Mechanical Systems and Signal Processing

Mechanical Systems and Signal Processing 160 (2021) 107933

Contents lists available at ScienceDirect

Mechanical Systems and Signal Processing

journal homepage: www.elsevier.com/locate/ymssp

Vibration modes and wave propagation of the rail under fastening constraint

Pan Zhang, Shaoguang Li, Alfredo Núñez, Zili Li *

Delft University of Technology, Section of Railway Engineering, Stevinweg 1, 2628 CN, Delft, the Netherlands

ARTICLE INFO

Article history:
Received 14 September 2020
Received in revised form 22 February 2021
Accepted 28 March 2021

Keywords:
Rail vibration modes
Wave propagation
Fastening constraint
Three-dimensional finite element model
Rail vibration control

ABSTRACT

This paper investigates three-dimensional (3D) rail vibrations under fastening constraint up to 5000 Hz and provides insights into rail vibration control by fastening parameters. A methodology is proposed, including experimental investigation and numerical simulations of rail vibrations. Three steps are considered: 1) experimental investigation of rail vibrations under fastening constraint; 2) validation and analysis of 3D finite element (FE) modeling of rail-fastening systems; 3) rail vibration control by fastening parameters. In Step 1, operating deflection shape (ODS) and synchronized multiple-acceleration wavelet (SMAW) measurements are applied to identify rail vibration modes and measure wave propagation characteristics under fastening constraint. In Step 2, a 3D FE model capable of reproducing the dynamic behaviors of rail-fastening up to 5000 Hz is developed to analyze rail vibrations and validated using measurements from Step 1. In Step 3, insights into the control of rail vibrations are gained by sensitivity analysis of fastening parameters using the validated 3D FE model from Step 2. The results indicate that (1) under fastening constraint, ODS measurement identifies vertical bending modes, longitudinal compression modes, and lateral bending modes of the rail with shifted frequencies and significantly reduced vibration amplitude compared to that of free rail. (2) Vertical wave attenuation of rail-fastening is relatively small between 1800 and 3600 Hz, and lateral wave attenuation presents a dominant peak at about 3800 Hz. (3) Compared to the vertical and lateral directions, the fastening system constrains the longitudinal rail vibrations less strongly. (4) The change of fastening stiffness and damping can control rail mode frequencies and their vibration amplitude, and influence the wave propagation velocities and attenuation along the rail.

1. Introduction

Rail vibrations play an essential role in wheel-rail dynamic interaction. Problems in the field of railway systems, such as short pitch corrugation and rolling noise, are closely related to rail vibrations. Hempelmann and Knothe [1] and Grassie [2] reported that the rail vertical 'pinned-pinned' mode was the wavelength-fixing mechanism of short pitch corrugation. Li et al. [3] concluded that the rail longitudinal vibration modes were dominant for short pitch corrugation initiation and consistency between the longitudinal and vertical modes determines its continuous growth. Rail vibrations can also be seen as the superposition of a series of vibrational waves [4]. Thomson et al. [4–6] linked the decay rate of the waves along the track

* Corresponding author.
E-mail address: Z.Li@tudelft.nl (Z. Li).

https://doi.org/10.1016/j.ymssp.2021.107933
0888-3270/

with noise radiation and reported that the vibrational waves in the rail were dominant for wheel-rail rolling noise in 500–1600 Hz, and generally remained important in higher frequencies up to 5000 Hz. Therefore, effective control of rail vibration modes and wave propagation may provide root-cause solutions to these vibration-related problems, for instance, by parameter optimization of fastenings [7], utilization of vibration absorber [8–10], and under sleeper pad [11]. This paper aims to provide insights into rail vibration control by fastening parameter design.

Fastenings impose significant constraints on rail vibrations. Fastenings mainly consist of two components: railpads and clamps. Railpads are resilient material components that are placed in between the rail and the sleeper to add elasticity to the track. Clamps fix the rail to the sleeper to ensure that the rail remains attached to the sleeper under train loads. Many studies have reported that the mechanical properties of railpads are nonlinear and depend on preload, excitation frequency, excitation amplitude, temperature, and aging [12–16]. The fastening models have been improved to consider the nonlinearity of railpads, from the simple Kelvin-Voigt (KV) model [17] to Poynting-Thomson (PT) model [18], Prony series model [16], fractional derivative model [19,20], and solid railpad model [21]. Ilias [7] and Egana et al. [22] studied the influence of railpad stiffness on corrugation development and found that the softer railpads can mitigate the corrugation growth compared to the stiffer ones. Thomson et al. [23] investigated the effect on the rolling noise of nonlinear railpad stiffness parameters, and the results indicated that stiffer railpads caused more considerable attenuation of rail vibration along the track and thus reduced the rail-radiated noise. Wei et al. [24] reported that the temperature- and frequency-dependent properties of railpads influenced the vertical accelerations of the rail above 315 Hz in high-speed vehicle-track coupled systems. Oregui et al. [25] performed a sensitivity analysis of railpad parameters on vertical track dynamics, and the derived receptance under different clamp loads and temperature could be used to monitor the fastenings in-service conditions.

Overall, most work mentioned above has explicitly or implicitly studied the vertical rail vibrations under fastening constraint because the wheel-rail excitation mainly acts in the vertical direction. Some researchers have also investigated the lateral rail vibrations under the fastening constraint for studying wheel-rail rolling noise [4,26]. However, the effect of fastening constraint on longitudinal rail vibrations have been barely reported in the literature. Therefore in this paper, we proposed a methodology to comprehensively investigate rail vibrations under fastening constraint in three dimensions (3D) and provide insights into rail vibration controls by fastenings design.

When considering three-dimensional rail vibrations, multiple rail vibration modes occur, and they are coupled together [27], making the mode identification more challenging than the uncoupled modes in a single direction. The dispersion and attenuation of the vibrational waves in the rail also make the wave measurement more difficult [4,27,28]. ODS and SMAW measurements were conducted in this paper to address these two issues. Compared to commonly-used frequency response function (FRF) measurement [26,29,30] for only deriving mode frequencies, ODS measurement has the advantage in identifying coupled vibration modes by obtaining both the mode frequencies and shapes. SMAW approach is capable of measuring wave propagation and dispersion in the rail from the synchronized acquisition of rail accelerations in multiple positions. In this paper, group velocities and the attenuation coefficient of the waves in the rail under fastening constraint are estimated.

When modeling high-frequency rail vibrations, analytical beam or plate models [31–33] are only valid up to 1500 Hz with an assumption of constant cross-section. The 2.5D FE model [34,35] and 3D FE model [36] can both consider rail cross-section deformation and thus are capable of accurately reproducing high-frequency rail vibrations. Compared to the 2.5D FE model, the 3D FE model has the advantage that it is able to simulate nonlinear wheel-rail dynamic contact, which is important to study wheel-rail rolling noise and short pitch corrugation. Oregui et al. [36] modeled the fastenings with multiple one-dimensional spring-damper elements to reproduce vertical track dynamics within 3000 Hz. In this paper, we extend the fastening model from one-dimensional to three-dimensional, and examine its validity in three directions up to 5000 Hz which cover the frequency interest of both short pitch corrugation and rolling noise.

This paper proposes a systematic methodology to investigate 3D rail vibration and control under fastening constraint. Through this methodology, rail vibration modes under fastening constraint can be identified by ODS measurement, and wave propagation characteristics can be measured by the SMAW approach. Insights into rail vibration control can be gained through sensitivity analysis of fastening dynamic parameters using a 3D FE model. The structure of this paper is as follows. Section 2 describes the methodology of this paper, including experimental investigation and numerical simulations. Section 3 presents the experimental results of ODS and SMAW measurements. Section 4 examines the validity of the proposed 3D FE rail-fastening model by comparison with measurements. Section 5 shows the control of rail vibration modes and wave propagation characteristics through the sensitivity analysis of fastening parameters. Section 6 discusses the relationship between the laboratory and in situ tests of rail vibrations under fastening constraint. The main conclusions and lines of further research are presented in Section 7.

2. Methodology

In this section, we describe a systematic methodology for studying rail vibration modes and wave propagation under fastening constraint. This methodology includes three steps: 1) experimental investigation of rail vibrations under fastening constraint; 2) the validation and analysis of 3D FE modeling of rail-fastening; and 3) rail vibration control by fastening parameters. In Step 1, an experimental setup consisting of rail-fastening is constructed in the laboratory. ODS and SMAW measurements are conducted to identify rail vibration modes and measure wave propagation characteristics under fastening constraint. In Step 2, a 3D FE model of rail-fastening is developed and validated by the ODS and SMAW measurement results.

With the simulation model, a better understanding of the rail vibrations in the experimental results are obtained. In Step 3, insights into rail vibration control are gained through sensitivity analysis of fastening dynamic parameters. The flowchart of the methodology is shown in Fig. 1.

2.1. Experimental investigation

2.1.1. Experimental setup

The experimental setup mainly consists of three parts: a rail, fastenings, and a standard 'I-cross section' steel beam, as shown in Fig. 2. The 4.97 m long UIC 54E1 rail was constrained on the beam by nine fastenings every 0.6 m, which is the fastening spacing in the field track. The fastening includes two components: railpads and Vossloh W-shaped tension clamps

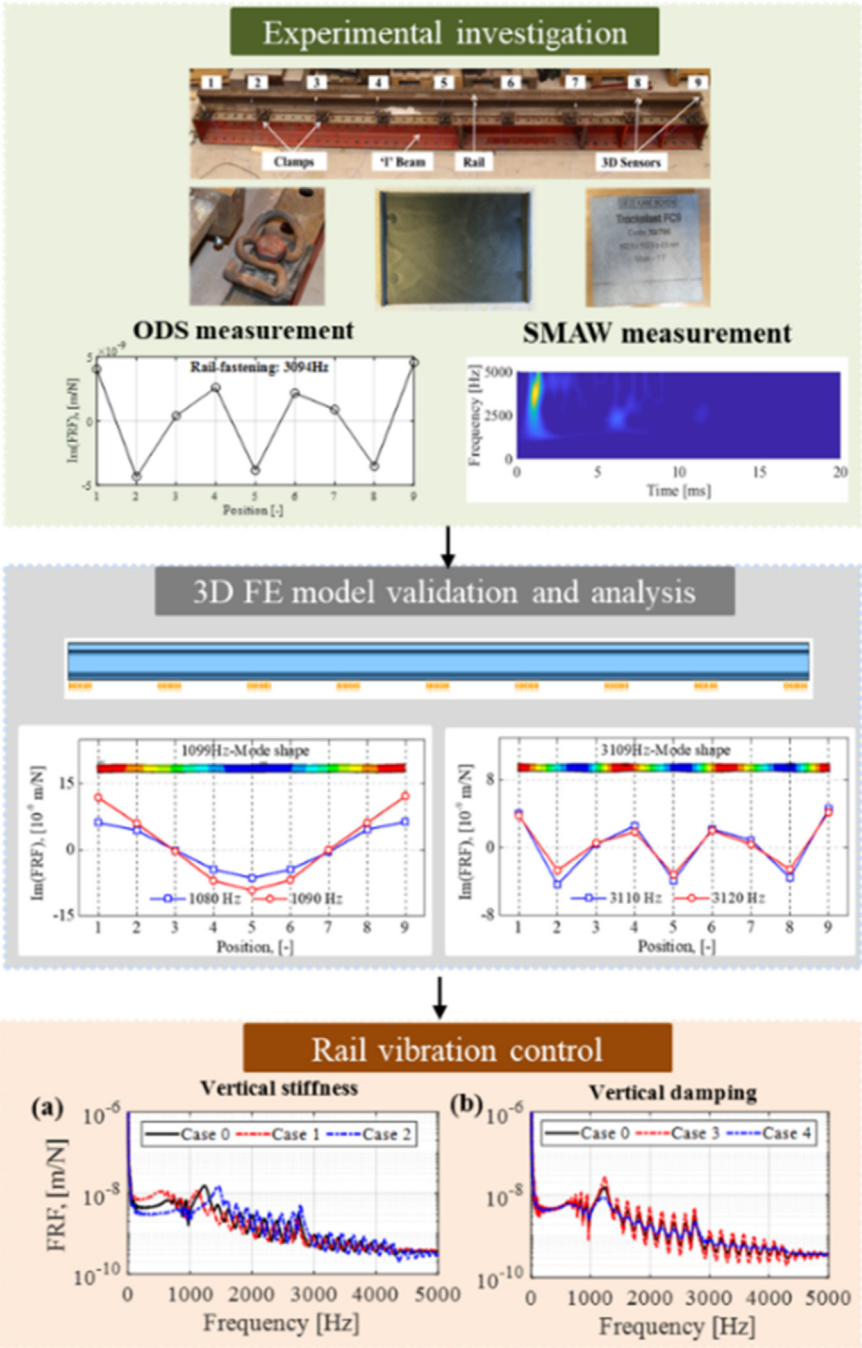

Fig. 1. Flowchart of the methodology.

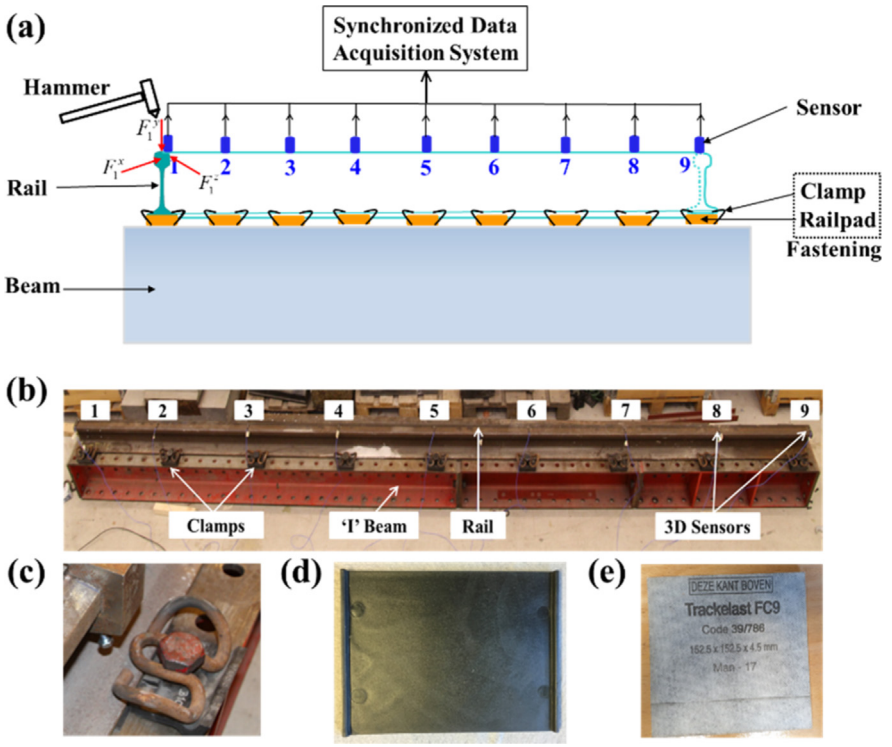

Fig. 2. Experimental setup. (a) Schematic drawing; (b) setup in the laboratory; (c) Vossloh W-shaped tension clamps; (d) Zw692-4 railpad; (e) FC9 railpad.

(Fig. 2c). Railpads were placed between the rail and the beam to provide elasticity. The W-shaped clamps were used to fix the rail on the beam. Each clamp was tightened by a torque of 240 Nm resulting in a preload of 20 kN, which is a toe load typically applied in field track. Two types of railpads, harder Zw692-4 (Fig. 2d) and softer FC9 (Fig. 2e), were tested in this setup, which is commonly used in the mainline of the Dutch railway network.

The sensor distribution in this setup is the same as in [27]. Nine 3D accelerometers (PCB 356B21, denoted as 1–9 in Fig. 2) were glued on the railhead surface with an approximately 0.6 m spacing. The smallest wavelength of the measurable modes by this sensor distribution is twice the sensor spacing. The responses of the nine accelerometers are denoted as follows,

$$a_i(t) = [a_i^x(t),\ \ a_i^y(t),\ \ a_i^z(t)]^T, \quad i = 1, 2, ..., 9 \tag{1}$$

where a_i(t) is the vector with responses of the i^{th} accelerometer, which includes three components a_i^x(t), a_i^y (t), a_i^z (t) in the longitudinal, vertical, and lateral directions, respectively. The experimental setup is used to obtain both the ODS and SMAW measurements. For the ODS measurement, all accelerometers are used to get the highest wavenumber resolution. For SMAW measurement, which is capable of identifying wave propagation and dispersion in the rail, only accelerometers 1, 5, and 9 are used.

A small hammer (PCB 086C03) with a steel tip was used to excite the rail in the high-frequency range. The excitation positions were as close as possible to the 3D accelerometer 1. Accelerometer 1 is at one of the free rail ends where the mode shapes have maximum deformation and thus the rail vibration modes can be excited with larger energy. In the real track, the rail ends are often constrained by, such as joints and welds, and the rail may have mode shapes and frequencies different from rails with free ends at the same wavelength/number. Impacts were conducted in the longitudinal, lateral, and vertical directions, recorded as $F_1^x(t)$, $F_1^y(t)$, $F_1^z(t)$, as shown in Fig. 2a. A synchronized data acquisition system recorded the excitation and the response signals. Five impacts in each direction were measured, with a sampling frequency of 51200 Hz. The reliable range of the impact forces and repeatability of the signals were checked as in [26], and they were valid up to 5000 Hz.

Compared to the field track, this setup did not include the sleepers, ballast, and other substructure components. These track components mainly contribute to the track dynamics in a lower frequency range than 400 Hz [32,37,38]. Instead, a steel beam was used as rail support in this setup, which has two advantages. Firstly, the rail support conditions were simplified compared to practice and make it easier to identify the effect of fastening constraint on rail vibrations without the influence of sleeper and ballast. Secondly, this beam support has much larger mass and stiffness, making it possible almost completely to suppress rail vibration modes by rail constraint design. Besides, a short length of rail (4.97 m) was chosen in this setup for the laboratory test while in the field, it usually is much longer. The influence of these differences between laboratory and field measurements on rail vibration modes and wave propagation will be discussed in Section 6.

2.1.2. ODS measurement method

ODS measurement is employed to identify different rail vibration modes. The ODSs are measured from a set of FRFs, which can be divided into two steps. The first step is to calculate the FRFs at different accelerometers by the following formula [39]:

$$\mathrm{FRF}_i^y(f) = \frac{S_{a_i^y F_1^y}(f)}{S_{F_1^y F_1^y}(f)(2\pi f)^2} \tag{2}$$

where $\mathrm{FRF}_i^y(f)$ is vertical FRF of accelerometer i; $S_{a_i^y F_1^y}$ is the cross-spectrum between the acceleration aiy(t), and force F1y (t), and $S_{F_1^y F_1^y}$ is the auto-spectrum of the force F1y(t). The FRFs are complex-valued functions. In the second step, the ODSs of rail displacement responses are taken as the spatial distribution of the imaginary parts of the FRFs, as follows [40]:

$$\mathrm{ODS}^y(f) = [Im(\mathrm{FRF}_1^y(f)),\ Im(\mathrm{FRF}_2^y(f)), \ldots,\ Im(\mathrm{FRF}_9^y(f))] \tag{3}$$

where $\mathrm{ODS}^y(f)$ is vertical ODS at frequency f. When the frequency is one of the natural rail frequencies, the ODS will closely approximate the mode shape [40]. The longitudinal and lateral FRFs and ODSs,$\mathrm{FRF}_i^x(f)$, $\mathrm{FRF}_i^z(f)$, $\mathrm{ODS}^x(f)$, $\mathrm{ODS}^z(f)$, can be obtained with the same method. One example to explain the procedure of ODS measurement in detail can be found in [27].

2.1.3. SMAW measurement method

SMAW measurement is applied to study wave propagation and dispersion in the rail. Wave propagation signals along the rail under hammer excitation are non-stationary and contain many frequency components. The continuous wavelet transform (CWT) is used to decompose these signals, which offers a good time and frequency resolution. In the CWT, the convolutions of the analyzed signal are calculated with a group of scaled and shifted wavelet functions. The wavelet coefficients $W_n(s)$ of the analyzed signal x_n can be represented as follows [41]:

$$W_n(s) = \sum_{n'=0}^{N-1} x_{n'} \psi^* \left[\frac{(n'-n)\delta_t}{s}\right] \tag{4}$$

where Ψ is the mother wavelet, s is the wavelet scale, N is the number of points in the time series, $n' = 0, \ldots, N-1$, δ_t is the time step, n is the continuous variable for the translation, $*$ presents a complex conjugate, and $\psi^*\left[\frac{(n'-n)\delta_t}{s}\right]$ is a family of wavelets deduced from the mother wavelet by various translation and scaling steps. Here, the Morlet function is employed as the mother wavelet [42]. The wavelet power spectrum (WPS) is calculated by $\left|W_n^2(s)\right|$. SMAW measurement refers to the measured WPSs of synchronized accelerations, in this paper, at positions 1, 5, and 9 (see Fig. 2). Among them, positions 1 and 9 are at the two rail ends where the wave vibration energy is stronger than the other positions because of the free boundaries. Therefore, the acceleration signals at these two positions will be used to calculate group velocities and attenuation coefficient of the waves because of the larger signal-to-noise ratio. Position 5 is in the middle of the rail. By analyzing accelerations signals at these three positions, the wave propagation along the rail can be clearly traced [27].

From WPSs, it is possible to estimate group velocity and attenuation coefficient of the waves in the rail under fastening constraint, as shown in Fig. 3. Firstly, WPSs of acceleration signals at the two rail ends are calculated. Then one frequency f_j (i.e., 2500 Hz) is chosen in the vertical WPSs, indicated by the white solid lines in Fig. 3b. The first peaks A_1 and A_2 at time t_1 and time t_2 are detected from the WPSs (see the red triangles in Fig. 3b), which are the first arrivals of the waves at the chosen frequency. There is a time difference dt between these two peaks, during which the waves propagate through the rail length (L). Therefore the vertical group velocity v_g^y at f_j is calculated as follows,

$$v_g^y(f_j) = \frac{L}{t_2(f_j) - t_1(f_j)} \tag{5}$$

Then, wave energy attenuation in the rail is estimated from the peak amplitude A_1 relative to A_2. A linear attenuation coefficient β_y is used to describe the wave decay per meter along the rail in the vertical direction [43], as follows,

$$\beta_y(f_j) = \frac{20\log_{10}(A_1(f_j)/A_2(f_j))}{L} \tag{6}$$

Afterward, we select the next frequency to study f_{j+1} and repeat the procedure above. At some frequencies, the vibration energy of the waves is small and peaks like in Fig. 3b may not be accurately detected from the WPSs. For these cases, the group velocity and attenuation coefficient are not estimated, so these are not considered in the final analysis. The longitudinal and lateral v_g^x, v_g^z and β_x, β_z can be obtained with the same method.

2.2. 3D FE model

A 3D FE model of rail-fastening was developed with ANSYS, as shown in Fig. 4. The rail was modeled with 8-node solid elements with a length of 4.97 m. The rail profile was measured by a 3D laser HandyScan with a high resolution of 30 um.

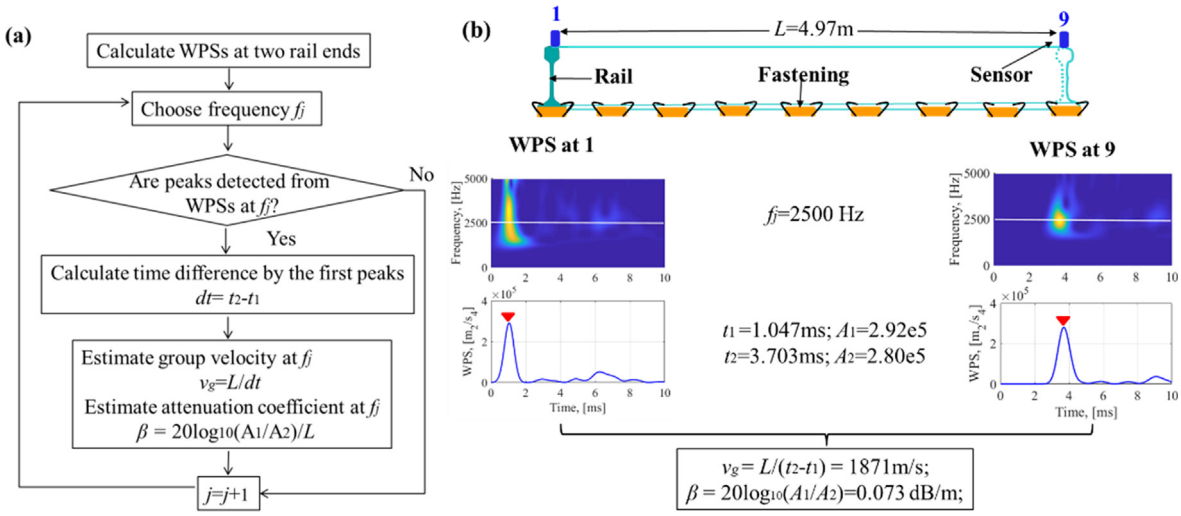

Fig. 3. The algorithm to measure group velocity and attenuation coefficient from WPSs. (a) Flowchart of the algorithm. (b) Example of the algorithm for a selected frequency f_j. The white line in (b) shows WPSs at 2500 Hz. The red triangles indicate the detected first peaks from WPSs at 2500 Hz.

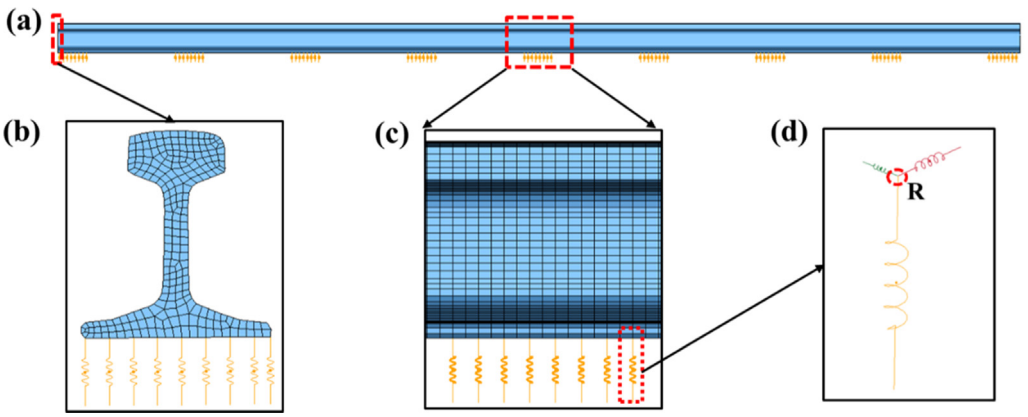

Fig. 4. Overview of FE rail-fastening model. (a) Rail-fastening model; (b) cross-section of rail-fastening model; (c)side view of the rail-fastening model; (d) three spring-damper elements at one rail node.

The rail cross-section was discretized with an equal element edge length of 4 mm, as shown in the left corner of Fig. 4. The longitudinal element size was 10 mm. This meshing method, in terms of the mesh size, was determined after a comparison of five different meshing methods in [27]. The meshing is thus a good compromise between simulation time and numerical accuracy. The rail material was treated as elastic isotropic with Young's modulus of 210 Gpa, Poisson's ratio of 0.3, and a density of 7850 kg/m^3. Free boundary conditions were applied to the two rail ends. The fastenings were modeled with multiple linear spring-damper pairs in the vertical, longitudinal, and lateral directions, which is an extension of the fastening model in [36]. Specifically, the fastening model consists of 72 spring-damper pairs in each direction, divided into nine rows (lateral direction of the rail in Fig. 4b) and eight columns (longitudinal direction of the rail in Fig. 4c). Fig. 4d shows three spring-damper elements at one rail node (marked by R). One end of three spring-damper pairs was connected to the rail node R, and the other ends were fixed. The steel beam was not included in this model for vibration analysis because experimental results indicated that its vibration was approximately 1/10 smaller compared to that of the rail and could thus be considered as stationary.

The hammer tests were numerically reproduced by an implicit-explicit sequential approach [36]. First, in the implicit calculation, the rail-fastening reached an equilibrium state under gravity. Subsequently, the nodal displacement from the implicit calculation was input as the initial state of the explicit simulation. In the explicit calculation, the impact force of the small hammer was modeled by a triangular force with a zero magnitude at t_0, a maximum magnitude at t_1 and a vanishing magnitude at t_2, as in [36]. The adopted time step is small enough (287 ns) to ensure the stability of the explicit integration. The stiffness and damping parameters of the fastenings were derived by best fitting the simulations to the measurement results

of railpad Zw692-4, which will be shown in Section 4. These parameters and the nominal material properties of the rail are listed in Table 1.

2.3. Rail vibration control by fastening parameters

Sensitivity analysis of fastening parameters is performed via the 3D FE rail-fastening model to gain insight into rail vibration control, as shown in Fig. 5. The fastening parameters are defined as a vector u, which serve as input for the 3D FE rail-fastening model.

$$u = [k_x, d_x, k_y, d_x, k_z, d_z]^T \tag{7}$$

where k_x, k_y, k_z are the fastening stiffness in the longitudinal, vertical, and lateral directions, and d_x, d_y, d_z are the fastening damping in the longitudinal, vertical and lateral directions. The output y of the 3D FE rail-fastening model indicates the estimation of the set of accelerations a_i i = 1,. . .,9, FRFs, ODSs, group velocities (v_g), and attenuation coefficients (β).

$$\begin{aligned}
&y = \{a(t),\ \mathrm{FRF}(f), \mathrm{ODS}(f),\ v_g(f),\ \beta(f)\}\\
&a(t) = \{a_1(t), ..., a_9(t)\}\\
&\mathrm{FRF}_i(f) = \{\mathrm{FRF}_i^x(f), \mathrm{FRF}_i^y(f), \mathrm{FRF}_i^z(f)\}\\
&\mathrm{FRF}(f) = \{\mathrm{FRF}_1(f), ..., \mathrm{FRF}_9(f)\}\\
&\mathrm{ODS}(f) = \{\mathrm{ODS}^x(f), \mathrm{ODS}^y(f), \mathrm{ODS}^z(f)\}\\
&v_g(f) = \left\{v_g^x(f), v_g^y(f), v_g^z(f)\right\}\\
&\beta(f) = \{\beta_x(f), \beta_y(f), \beta_z(f)\}
\end{aligned} \tag{8}$$

with t during the simulation time, and f in the frequency range of importance for the application (0 to 5000 Hz). The 3D FE simulation requires parameters that are obtained from the experimental setup (such as impact forces) and literature (such as the number of elements, rail parameters, etc.). Those parameters are included in the parameter vector θ_{FE}. Then, given the input vector of parameters of the fastening, the output of the rail-fastening model is given by:

$$y = f_{\text{rail - fastening}}(u, \theta_{FE}) \tag{9}$$

The sensitivity analysis is conducted by comparing changes in the output when including changes in the fastening parameters with respect to nominal parameters. Nominal fastening parameters u_{nominal} are as in Table 1, obtained by solving the inverse problem by fitting the output of the model to measurements from Step 1. A nominal output (y_{nominal}) of the rail-fastening system is obtained as follows:

$$y_{\text{nominal}} = f_{\text{rail - fastening}}(u_{\text{nominal}}, \theta_{FE}) \tag{10}$$

Then, we select one fastening parameter, for example, longitudinal stiffness k_y, and define two inputs

$$\begin{aligned}
u_A &= u_{\text{nominal}} + u_{\Delta A}^{k_y}\\
u_B &= u_{\text{nominal}} + u_{\Delta B}^{k_y}
\end{aligned} \tag{11}$$

with

$$\begin{aligned}
u_{\Delta A}^{k_y} &= [0, 0, +\Delta A, 0, 0, 0]^T, \quad \Delta A \geqslant 0\\
u_{\Delta B}^{k_y} &= [0, 0, -\Delta B, 0, 0, 0]^T, \quad \Delta B \geqslant 0
\end{aligned} \tag{12}$$

where ΔA and ΔB are variations of the specific parameter. The outputs y_A, y_B with parameters u_A and u_B are derived using the 3D FE model,

Table 1
The values of parameters used in the model.

Component	Parameter	Value
Rail	Young's modulus	210 Gpa
	Poisson's value	0.3
	Density	7850 kg/m^3
Fastening with Zw 692 railpad	Vertical stiffness	600 kN/mm
	Vertical damping	16 kNs/m
	Longitudinal stiffness	160 kN/mm
	Longitudinal damping	6 kNs/m
	Lateral stiffness	160 kN/mm
	Lateral damping	20 kNs/m

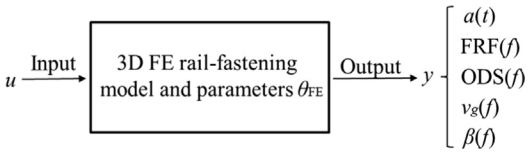

Fig. 5. Block diagram representation of the FE rail-fastening model.

$$y_A = f_{\text{rail - fastening}}(u_A, \theta_{\text{FE}})$$
$$y_B = f_{\text{rail - fastening}}(u_B, \theta_{\text{FE}}) \tag{13}$$

Finally, y_{nominal}, y_A and y_B are compared to determine the effect of the fastening parameter (i.e., longitudinal stiffness) on rail vibrations. Thus, the effect on the rail vibration control by this parameter is determined, for instance, including the frequency shift and peak amplitude in the FRFs, wave velocities and attenuation in the rail.

3. Experimental results

In this section, the experimental results of the rail-fastening are presented. Results are compared with those of the free rail to study the effect of fastening constraint on rail vibrations.

3.1. Results of ODS measurement

Fig. 6 shows the FRFs of rail-fastening with Zw692-4 railpads and free rail at accelerometer 1 in the vertical, longitudinal, and lateral directions up to 5000 Hz. The set of major peaks in the vertical FRF of free rail (see Fig. 6a) correspond to the rail vertical bending modes [27]. The fluctuation amplitude of vertical FRF is much reduced with the inclusion of fastening constraint, compared to those of the free rail. The distinguishable fluctuation peaks of the rail-fastening system are only observed around 1500 and 3300 Hz. The frequencies of the fluctuation peaks are shifted, e.g., from 2283 Hz or 2495 Hz of free rail to 2398 Hz of the rail-fastening case (indicated by red arrows in Fig. 6a). In order to identify the rail vibration modes related to these peaks, the corresponding ODSs are derived and shown in Fig. 7a, b, and c. It can be seen that the ODS of rail-fastening at 2398 Hz shares a similar shape with the ODS of free rail at 2283 Hz, and different from that at 2495 Hz. This indicates the peak at 2398 Hz corresponds to one vertical bending mode, and its frequency is shifted from

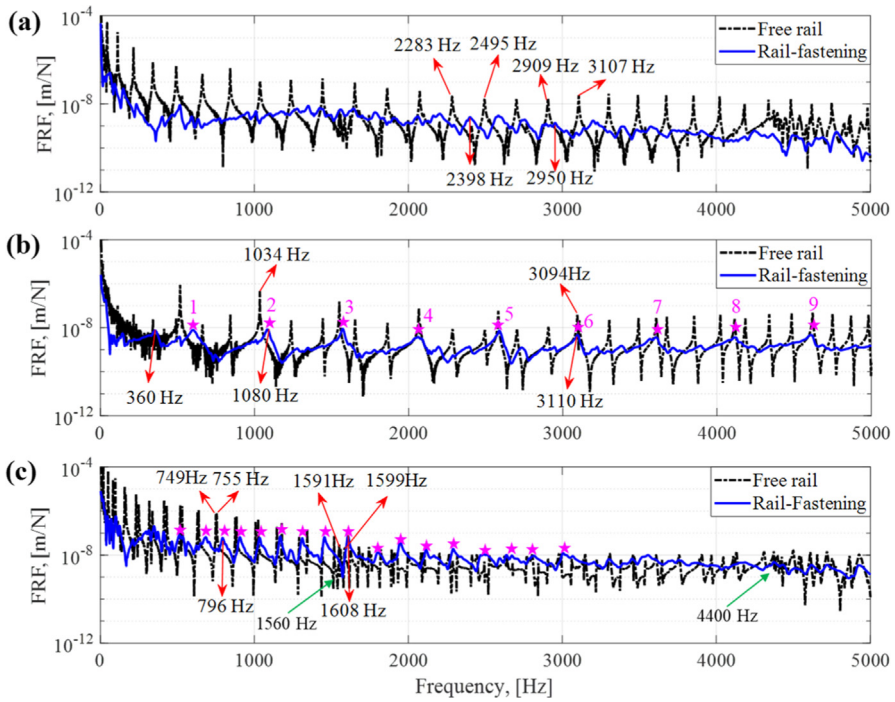

Fig. 6. FRFs at accelerometer 1 in the (a) vertical, (b) longitudinal (c) lateral directions. The red arrows in this figure show peak frequencies of the FRFs. The results of free rail are from [27].

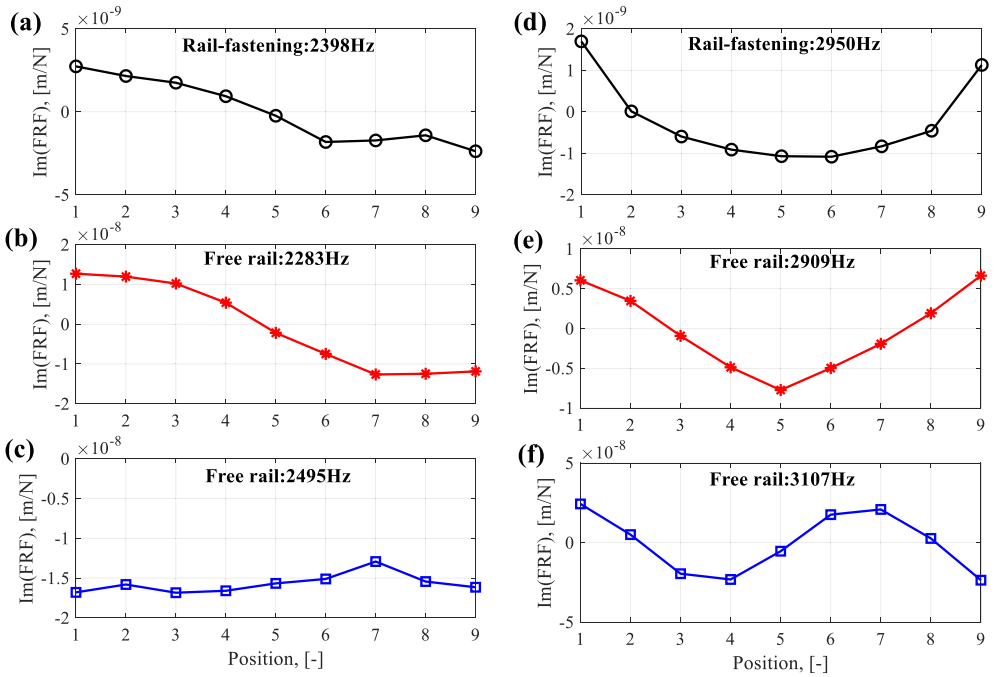

Fig. 7. Vertical ODSs: (a) rail-fastening at 2398 Hz, (b) free rail at 2283 Hz, (c) free rail at 2495 Hz, (d) rail-fastening at 2950 Hz, (e) free rail at 2909 Hz, (f) free rail at 3107 Hz.

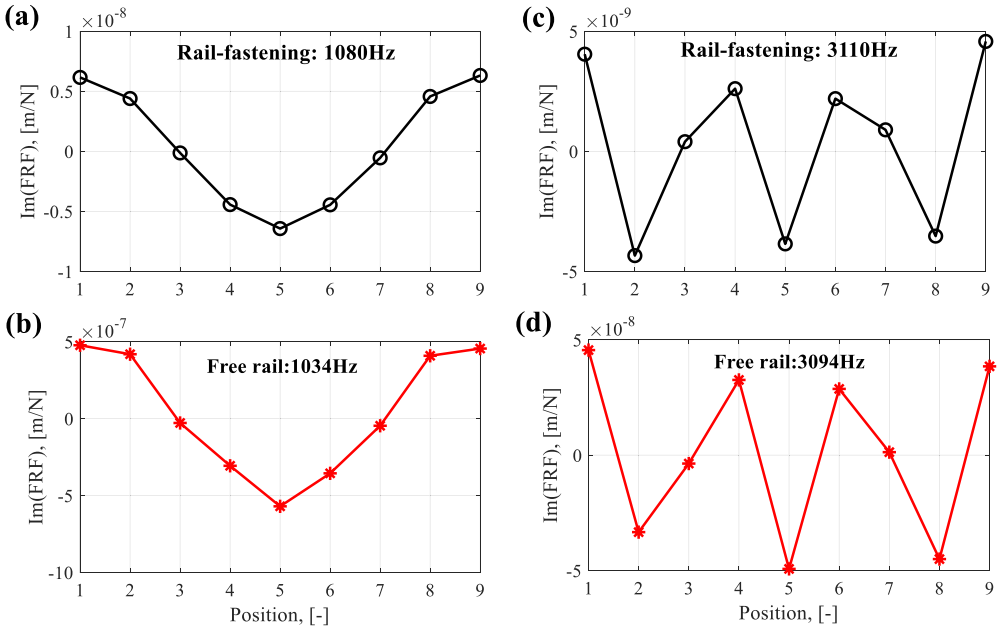

Fig. 8. Longitudinal ODSs: (a) rail-fastening at 1080 Hz, (b) free rail at 1034 Hz, (c) rail-fastening at 3110 Hz, (d) free rail at 3094 Hz.

2283 Hz to 2398 Hz under fastenings constraint. In Fig. 7d, e, and f, another example shows that the peak frequencies are shifted from 2909 Hz of free rail to 2950 Hz of rail-fastening, confirming that fastenings increase the vertical bending mode frequencies of the rail. Besides, it is found that at frequencies higher than 1000 Hz, the overall average trends of the FRFs are similar in these two cases, but the FRF of the rail-fastening is reduced at frequencies lower than around 1000 Hz. Compared to clearly distinguished vertical bending modes of free rail in the FRF below 1000 Hz, almost no peaks were observed in that of rail-fastening system, which should be caused by the fastening damping that dissipates the vibration energy.

In Fig. 6b, the major peaks in the longitudinal FRF of free rail correspond to longitudinal compression modes [27]. With the fastening constraint, one set of peaks (indicated by ★ and numbers) is still distinguishable in the frequency range of 0–5000 Hz, although their fluctuation amplitudes significantly decrease. It can also be observed that the frequencies of the first three peaks of free rail are shifted to the right, and the others are almost unchanged. One additional peak occurs in the longitudinal FRF of rail-fastening at around 360 Hz, which corresponds to the rail resonance mode on the longitudinal fastening stiffness. Fig. 8a and c show ODSs of rail-fastening at 1080 Hz and 3110 Hz. These have a similar shape to ODSs of free rail at 1034 Hz and 3094 Hz, respectively (see Fig. 8b and d). These results indicate that the peaks of rail-fastening correspond to longitudinal compression modes.

In Fig. 6c, the fluctuation amplitude of the lateral FRF of rail-fastening considerably decreases compared to that of free rail. The lateral FRF of free rail in Fig. 6c shows the coupling of four sets of major peaks, representing lateral bending, lateral torsion, web 1st bending and web 2nd bending modes, respectively [27]. Specifically, two sets of major peaks at 0–1560 Hz correspond to lateral bending and torsion modes, and at approximately 1560 Hz and 4400 Hz, with the supplement of web 1st and 2nd bending modes (indicated by two green arrows, respectively). However, with the inclusion of the fastening, only one set of major peaks (indicated by ★) can be identified between 300 Hz and 3000 Hz. Also, the frequencies of the peaks are shifted, e.g., from 749 Hz or 755 Hz of free rail to 796 Hz of rail-fastening. To identify the vibration modes of the rail-fastening, the corresponding ODSs are derived, as shown in Fig. 9a, b, and c. It can be seen from Fig. 9b and c that despite a marginal frequency difference of 6 Hz, the ODSs of free rail at 749 Hz and 755 Hz shows a significant difference, which corresponds to lateral bending mode and torsion mode, respectively. The ODS of rail-fastening at 796 Hz has a similar shape (Fig. 9a) to that of free rail at 749 Hz, indicating this peak represents a lateral bending mode. A similar result is observed in Fig. 9d, e, f that the ODS of rail-fastening at 1608 Hz resembles the ODS of free rail at 1599 Hz (lateral bending mode) rather than that at 1591 Hz (web 1st bending mode). We also checked other peaks and their ODSs and found that the remaining set of major peaks of the rail-fastening system correspond to lateral bending modes, and the fastening constraint probably suppresses the other three types of lateral modes occurring in the FRF of free rail.

Fig. 10 compares the FRFs of the rail-fastening system with two types of railpads, harder Zw692-4, and softer FC9. Overall, the vertical and lateral FRFs in these two cases are similar to each other below 4000 Hz, but present deviations at frequencies higher than 4000 Hz. Moderate differences are observed in the longitudinal FRFs at frequencies lower than 1500 Hz. For the softer FC9, the peak fluctuation amplitudes are larger, and the corresponding peak frequencies are smaller than those of harder Zw692-4.

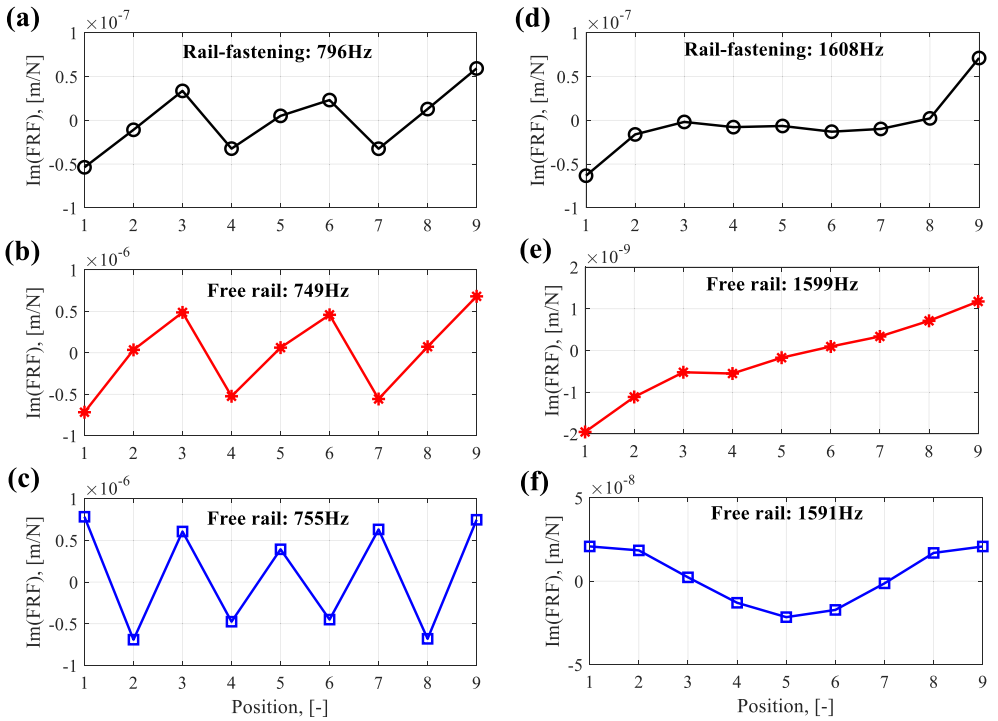

Fig. 9. Lateral ODSs: (a) rail-fastening at 796 Hz, (b) free rail at 749 Hz, (c) free rail at 755 Hz, (d) rail-fastening at 1608 Hz, (e) free rail at 1599 Hz, (f) free rail at 1591 Hz.

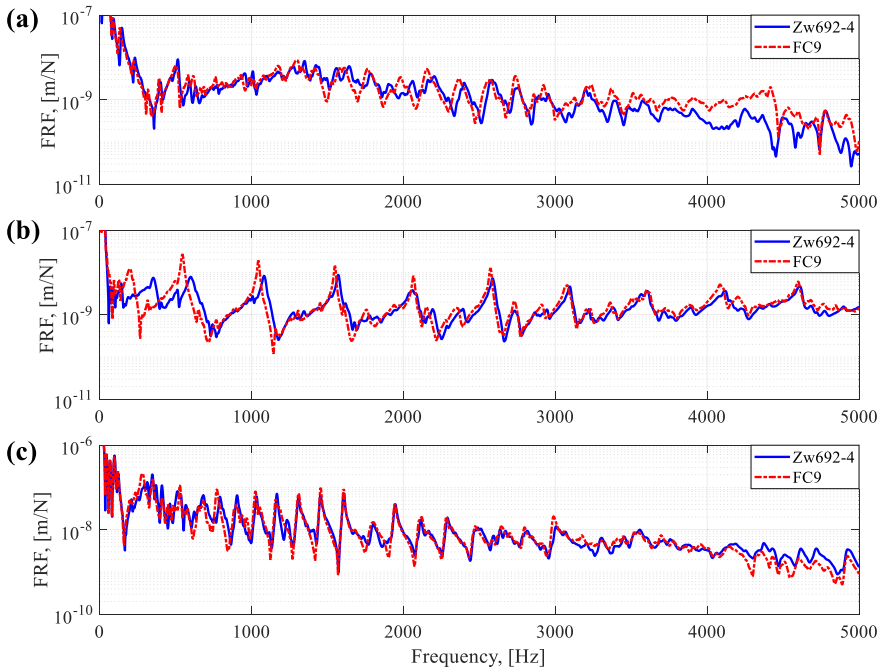

Fig. 10. FRFs with two railpad types at accelerometer 1 in the (a) vertical, (b) longitudinal (c) lateral directions.

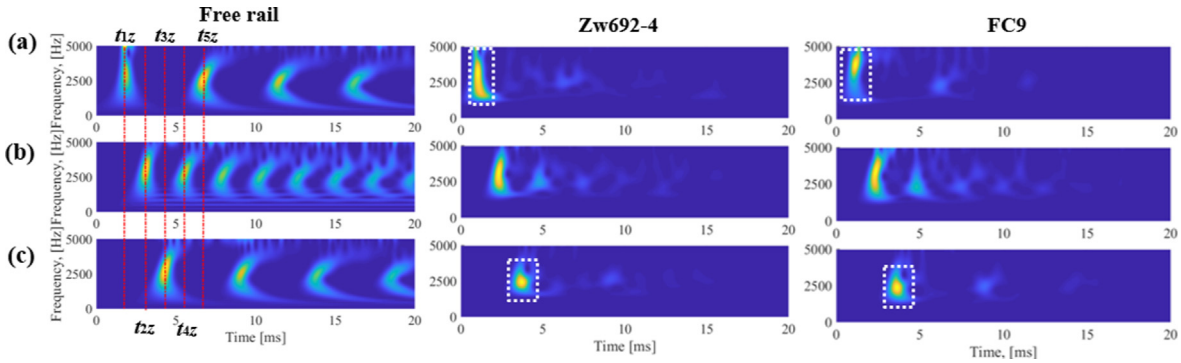

Fig. 11. Vertical WPSs at (a) accelerometer 1; (b) accelerometer 5; (c) accelerometer 9. The left, middle, right figures refer to free rail, rail-fastening with Zw692-4 and FC9, respectively. The red dash lines are the selected time.

3.2. Results of SMAW measurement

The WPSs of vertical accelerations of free rail and rail-fastening with railpads Zw692-4 and FC9 are shown in Fig. 11. Fig. 11a, b, and c correspond to the signals at accelerometer 1, 5, and 9, respectively. The color contrast indicates the amount of energy concentrated in a frequency range (the vertical axis) at a particular time (the horizontal axis). The wave envelope propagation along the free rail can be seen in the figures. At time t_{1z}, the hammer excites the rail near accelerometer 1. Then, the wave envelope propagates to accelerometer 5 at time t_{2z}, and to accelerometer 9 at time t_{3z}. After that, the waves reflect at accelerometer 9 and come back to accelerometer 5 at time t_{4z}, and to accelerometer 1 at t_{5z}. During propagation, the shapes of the wave envelope change to a '*C*' shape due to wave dispersion. With the inclusion of fastenings, the wave envelope can be seen propagating from accelerometer 1, through accelerometer 5 and to accelerometer 9. After that, the energy of the wave envelope becomes too low to be observed. This result indicates that the wave attenuation of the rail-fastening considerably increases compared to that of free rail. Additionally, we can see that the wave envelope of the rail-fastening at accelerometer 1 concentrates on a broader frequency band in about 1200–5000 Hz, but shrinks to a narrower frequency band in 1800–3600 Hz at accelerometer 9, as indicated by the white dashed rectangular in Fig. 11a and c. This phenomenon qualitatively suggests that the wave attenuation in 1800–3600 Hz is less significant than that in ranges 1200–1800 Hz and 3600–5000 Hz.

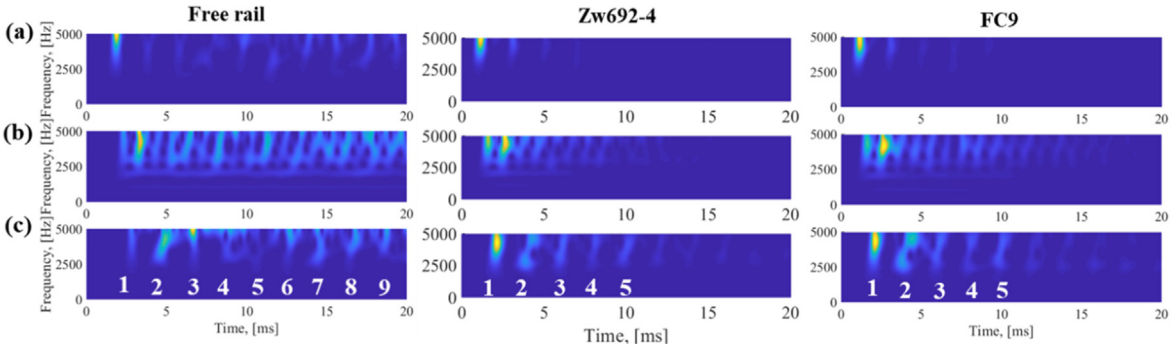

Fig. 12. Longitudinal WPSs at (a) accelerometer 1; (b) accelerometer 5; (c) accelerometer 9. The left, middle, right figures refer to free rail, rail-fastening with Zw692-4 and FC9, respectively. The number 1–9 in Fig. 12 indicates the number of wave envelopes.

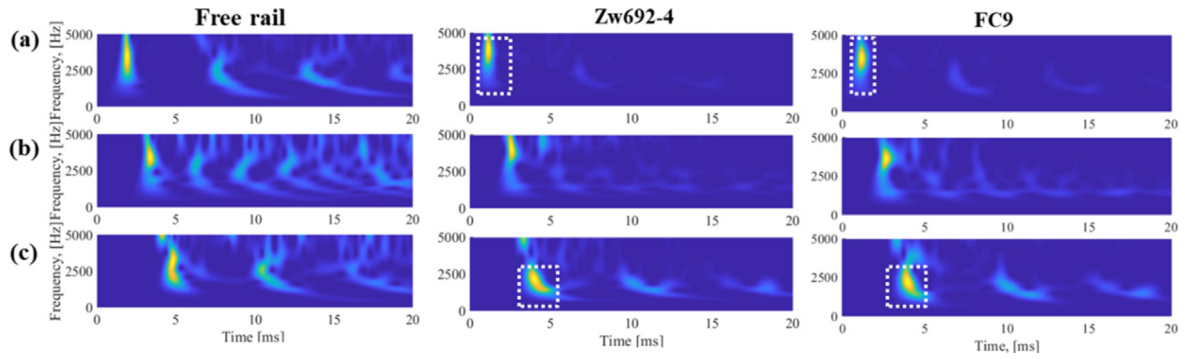

Fig. 13. Lateral WPSs at (a) accelerometer 1; (b) accelerometer 5; (c) accelerometer 9. The left, middle, right figures refer to free rail, rail-fastening system with Zw692-4 and FC9, respectively.

Fig. 12 shows the WPSs of the longitudinal acceleration signals. Because of the group velocity (around 5100 m/s) is larger than the vertical one (maximum 2000 m/s), more wave envelopes are observed in the longitudinal WPSs of free rail than those in vertical ones. With the fastening constraint, the number of clearly observable wave envelopes is reduced, e.g., from 9 to 5 in Fig. 12c, indicating that fastenings significantly increase the longitudinal wave attenuation.

The WPSs of the lateral waves are shown in Fig. 13. Similar to the vertical and longitudinal waves, the lateral waves are also considerably attenuated under fastening constraint. From the white dashed rectangular in Fig. 13a and c, it can be seen that the wave envelopes of rail-fastening at accelerometer 1 mainly concentrate on a higher frequency band of about 2500–5000 Hz, but change to about 600–2800 Hz at accelerometer 9. This result qualitatively indicates that the lateral wave attenuation in 600–2800 Hz is smaller than that at higher frequencies. Besides, one discontinuity zone in the wave envelope of rail-fastening is found between about 3000 Hz and 4000 Hz in Fig. 13c, suggesting that the wave attenuation is so strong that the lateral waves in this frequency range cannot propagate from position 1 to position 9.

The group velocities of rail-fastening with Zw692-4 and FC9 are measured and compared with those of free rail in Fig. 14. With the inclusion of fastenings, the vertical group velocity is significantly reduced at frequencies lower than about 1000 Hz, and one noticeable peak occurs at around 1150 Hz. This peak of harder Zw692-4 is more predominant than that of softer FC9. The longitudinal group velocity almost does not change in these three cases with a value of around 5100 m/s, corresponding to the propagation velocity of compression waves in solid guides, which is $\sqrt{E/\rho} = 5172$m/s, where E = 210 GPa, ρ = 7850 m/s for the rail material. The lateral group velocity curves of both railpads overlap almost entirely with each other and are larger than that of free rail above 2500 Hz.

Fig. 15 shows measured attenuation coefficients of the rail-fastening with Zw692-4 and FC9. The vertical attenuation coefficient firstly decreases from its lower frequency value to a minimum value (around 0 dB/m) at 2400 Hz, then increases to about 7 dB/m at 5000 Hz. These results agree with the observations in Fig. 11a and c, where vertical wave envelope shrinks to a narrower frequency band in 1800–3600 Hz at accelerometer 9 after propagation from accelerometer 1 because of the smaller attenuation in this frequency range. The longitudinal attenuation coefficient first drops from around 200 to 800 Hz, and then gradually goes up to about 4.5 dB/m at 5000 Hz. The lateral attenuation coefficient has a valley at about 1000 Hz and a dominant peak at about 3800 Hz. This peak frequency corresponds to the discontinuity zone in the wave envelope of rail-fastening in Fig. 13c. Compared to the harder Zw692-4, the vertical attenuation coefficient of the softer FC9 is lower before the valley at 2400 Hz and becomes higher afterward. The longitudinal attenuation coefficients show a

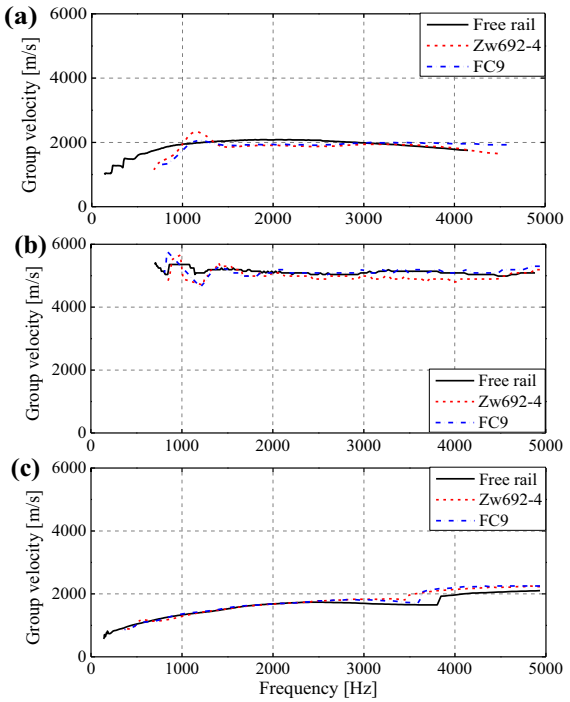

Fig. 14. Measured group velocity dispersion curves of free rail, rail-fastening with Zw692-4, and FC9 in the (a) vertical, (b) longitudinal, and (c) lateral directions.

similar level in these two cases. The lateral attenuation coefficient of harder Zw692-4 is averagely 1 dB/m larger than that of softer FC9.

4. Validation and analysis of 3D FE model

In this section, the proposed 3D FE rail-fastening model was validated by the experimental results of ODS and SMAW measurement from railpad Zw692-4. The dynamic parameters of fastenings were derived by best fitting the simulations to measurements. To better understand the experimental results, modal analysis of the FE model was performed, and the wavenumber-frequency dispersion curves were derived.

4.1. Validation of FRFs and ODSs

The closest fits of the simulated and measured FRFs at accelerometer 1 in the three directions are shown in Fig. 16. The overall tendencies and fluctuation amplitude from the simulations match the measurements well. The simulations identify almost all the peaks in the measured FRFs. Some differences are observed at lower frequencies (i.e., below 1000 Hz in the vertical direction, below 700 Hz in the lateral direction), which may be caused by the simplification of the fastenings in the simulation which were modeled by linear spring-damper elements. Taking the non-linear properties of fastenings (i.e. frequency-dependent) into consideration may improve the simulation results, which will be conducted in future research. Overall, good agreement has been achieved between simulations and measurements, indicating the proposed 3D FE model can accurately reproduce the dynamics behaviors of rail-fastening up to 5000 Hz.

Two examples of the simulated and measured ODSs in each direction are compared in Fig. 17. Fig. 17a, b are the vertical ODSs, Fig. 17c, d are the longitudinal ODSs and Fig. 17e, f are the lateral ODSs. Overall, good agreement is achieved between simulations and measurements in terms of frequencies and the shapes of ODSs. Slight differences are found in the amplitudes of the simulated and the measured ODS, e.g., the simulation slightly underestimates the vertical ODS amplitude at around 2950 Hz in Fig. 17b. These differences could be caused by the linear treatment of system components in the simulation while in the real situation, they are frequency-dependent [16].To better understand the results of the ODS measurement, the simulated mode shapes are also included in Fig. 17. The color contrast in the mode shapes indicates the relative deformations of the elements. Blue is the minimum deformations, and red is the maximum. The numbered black dashed-lines mark the nine sensor positions. It can be seen that the values of ODSs are consistent with the deformations of mode shapes: the larger ODS value corresponds to the larger deformation and vice visa. Additionally, it is noted that the ODSs com-

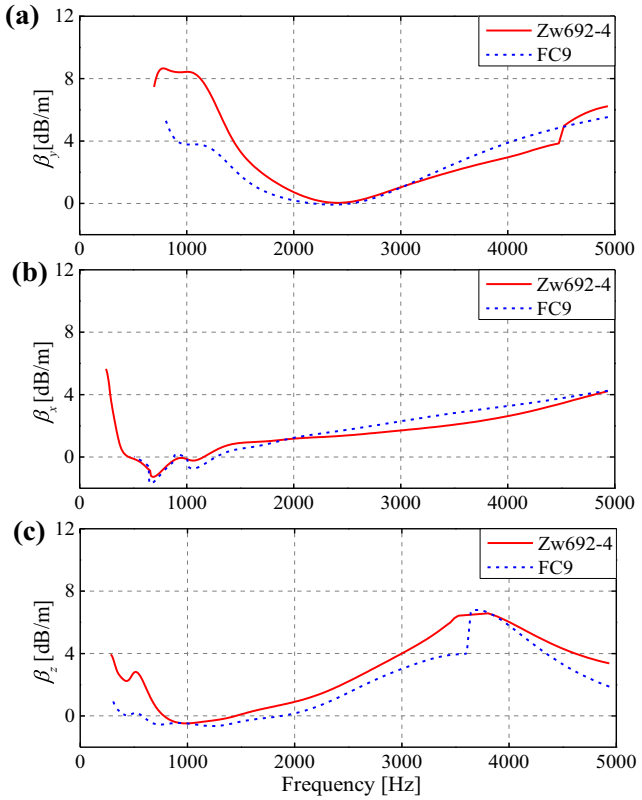

Fig. 15. Measured attenuation coefficients of rail-fastening with Zw692-4 and FC9 in the (a) vertical, (b) longitudinal, and (c) lateral directions.

pletely capture only the mode shapes of the longitudinal modes which have larger wavelengths. To identify the vertical and lateral modes in Fig. 17a, b, e, f, more sensors are needed to improve the wavelength/wavenumber resolutions.

4.2. Validation of group velocities and attenuation coefficient

The simulated group velocities and attenuation coefficients are compared with the measured ones in Fig. 18. Overall, good agreement is achieved between simulations and measurements in the three directions, indicating that the proposed model is capable of representing the wave propagation characteristics up to 5000 Hz. Some differences are observed at frequencies lower than 1000 Hz in Fig. 18a and c. These differences may be caused by the simplification of the rail support in the simulation (steel beam was not modeled). Slight differences above 3000 Hz in Fig. 18a and c might be related to the rail defects in the experimental setup.

4.3. Analysis of rail vibrations by wavenumber-frequency dispersion curves

To better understand the rail vibration modes and wave propagation characteristics, the wavenumber-frequency dispersion curves of vibrational rail waves are derived by modal analysis, as shown in Fig. 19. These waves include the vertical bending waves (I), longitudinal compression waves (II), and lateral bending waves (III) of free rail and rail-fastening system. The lateral torsion waves, web 1st bending, and 2nd bending waves are not included because they are not observed in the measured FRFs, see Fig. 6c.

Firstly, the wavenumber-frequency dispersion curves explain the frequency shift of the rail vibration modes observed from FRFs. It can be seen from Fig. 19 that fastening constraint increases the frequencies of the vertical bending waves compared to free rail, which explains that the peak frequencies of vertical FRF (Fig. 6a) are shifted to the right in the range 1500–3300 Hz. Fastening constraint also increases the frequencies of the longitudinal compression waves at lower wavenumber than about 1.5 rad/m, agreeing with the observation in Fig. 6b that the frequencies of the first three longitudinal modes are shifted to the right, and the others keep almost unchanged. Besides, it can be seen that the cut-on frequencies of waves I, II, and III rise to 615 Hz, 370 Hz, and 218 Hz from 0 Hz of free rail. The cut-on frequencies correspond to the rail resonance on the fastening stiffness [4].

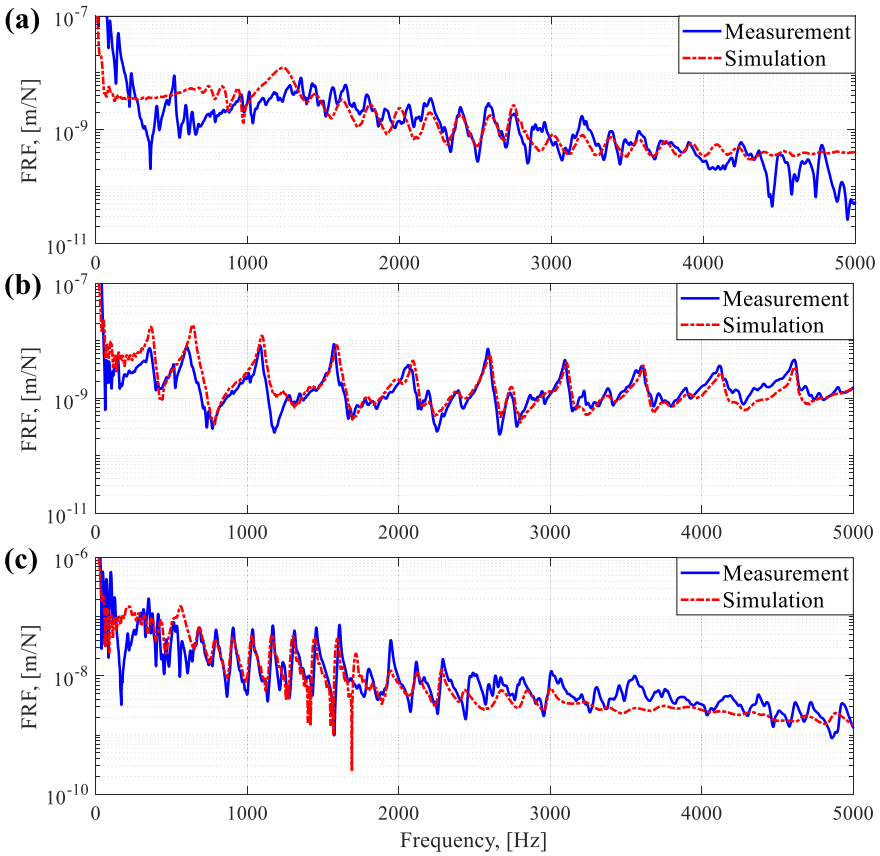

Fig. 16. Validation of FRFs in the (a) vertical (b) longitudinal and (c) lateral directions.

Secondly, the wavenumber-frequency dispersion curves provide more information about the group velocities. Group velocities can be estimated from wavenumber-frequency relations as follows [44]:

$$v_g = \frac{d\omega}{dk} = 2\pi \frac{df}{dk} \tag{14}$$

where v_g is group velocity, ω is the angular frequency, f is the ordinary frequency, and k is the wavenumber. It can be seen that group velocity is the tangential slope at a point on the wavenumber-frequency curve multiplied by 2π. From Fig. 19, it can be seen that at lower frequencies, close to the cut-on frequencies, the tangential slope of the wavenumber-frequency curves of the rail-fastening is smaller than those of free rail, resulting in smaller group velocities. At higher frequencies, tangential slopes of vertical (I) and longitudinal waves (II) are similar in these two cases, and therefore the group velocities change little under fastening constraint. The tangential slopes of lateral waves of rail-fastening increase at frequencies higher than 2500 Hz compared to free rail, corresponding to larger lateral group velocities. The estimations of the group velocities from the wavenumber-frequency curves provide a better understanding of the measurement results in Fig. 14.

5. Rail vibration control by fastening parameters

A sensitivity analysis of fastening parameters was performed to gain insight into rail vibration control. Based on the derived FRFs, rail vibration modes, wave group velocities and attenuation coefficient, a discussion over mitigation of short pitch corrugation and rolling noise by optimization of fastening parameters was included. The simulation cases are listed in Table 2. Case 0 is taken as a reference and applies the same fastening parameters as in Table 1, u_{nominal}. Other cases change one fastening parameter compared to reference Case 0, following the procedure in Section 2.3. For example, Case 1 reduces the vertical stiffness of Case 0 from 600 MN/m to 300 MN/m, and other parameters are kept the same.

5.1. Rail vibration modes

Fig. 20 shows the influence of fastening parameters on the FRFs. It can be seen from Fig. 20a that with the increase of vertical stiffness, the frequencies of vertical vibration modes are shifted to higher frequencies, and meanwhile, the FRF

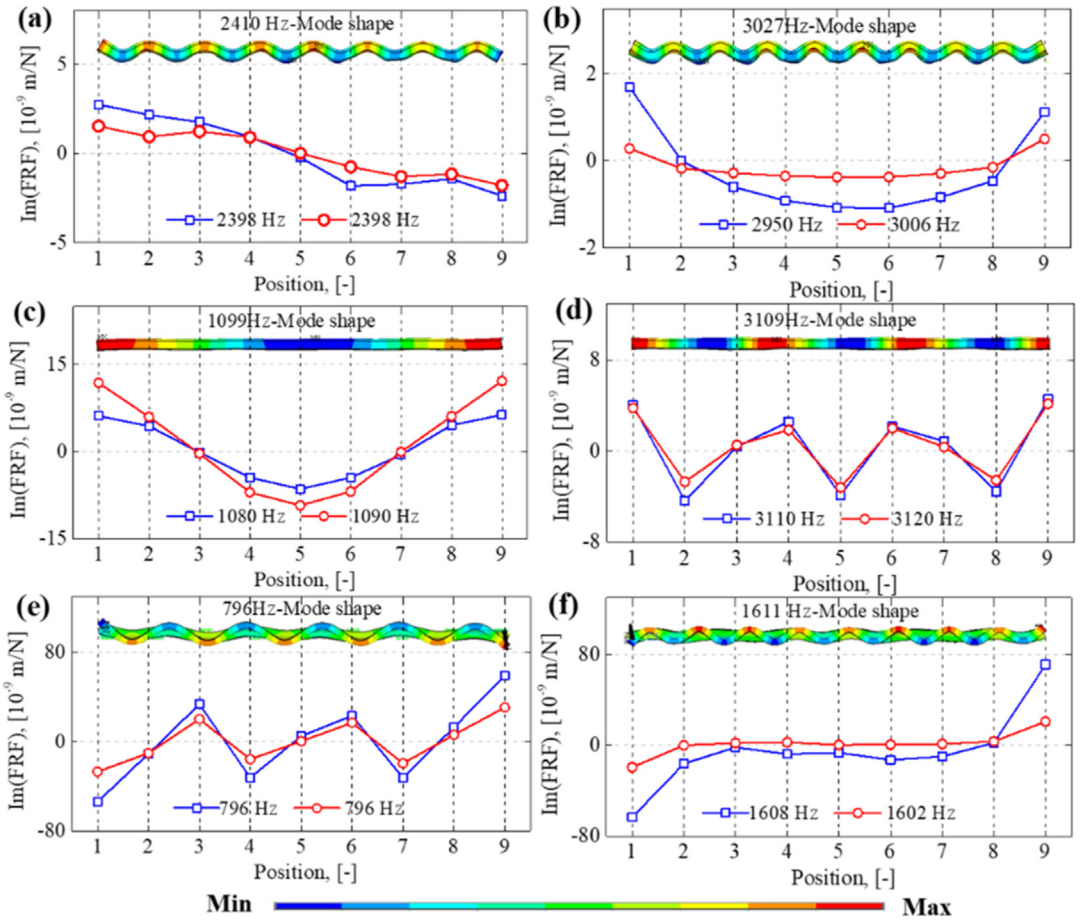

Fig. 17. Comparison of simulated (—□—) and measured (—○—) ODSs and mode shapes. (a) (b) in vertical direction; (c) (d) in longitudinal direction; (e) (f) in lateral direction.

amplitude is reduced at lower frequencies than 1000 Hz. The fluctuation amplitude of the modes does not change much in these three responses. Similar results in terms of frequency shift and FRF amplitude reduction are also observed in the longitudinal FRFs with different longitudinal stiffness (Fig. 20b) below 2000 Hz. At higher frequencies, the influence of longitudinal stiffness on FRFs is insignificant in these three cases. With the given three lateral stiffness, the lateral FRFs changes little, which may indicate that the lateral vibration modes are insensitive to the fastening stiffness. In all the three directions, the same trend of the influence of fastening damping is observed: larger damping leads to smaller fluctuation amplitude of the vibration modes.

The results in Fig. 20 provide insights into the control of rail vibration modes. For instance, when wheel-rail excitation frequencies are closer to the rail mode frequencies, strong resonance vibrations happen, which accelerate the track degradation. By optimization of fastening stiffness, the rail mode frequencies could be shifted to avoid the resonance. It is reported in [3] that the consistency between the longitudinal and vertical vibration modes determines the continuous growth of corrugation. Therefore by the design of the fastening longitudinal and vertical stiffness, it is expected to control this consistency, and the corrugation growth eventually. Increasing fastening damping effectively suppresses the vibration amplitude of rail modes in three directions, which is helpful for mitigation of track vibration in practice.

5.2. Wave propagation characteristics

Fig. 21 shows the influences of fastening stiffness on rail wave propagation characteristics in the three directions. With the increase of vertical stiffness, the vertical group velocity is significantly reduced below 3000 Hz, as shown in Fig. 21a. The vertical attenuation coefficient considerably increases before the valley at 2400 Hz and decreases at higher frequencies. A similar trend in terms of group velocity reduction and attenuation coefficient increase at low frequencies are also found in the longitudinal direction with longitudinal stiffness increase, as shown in Fig. 21c and d. Fig. 21e and f shows that the lateral group velocities and attenuation coefficient are insensitive to the change of lateral stiffness.

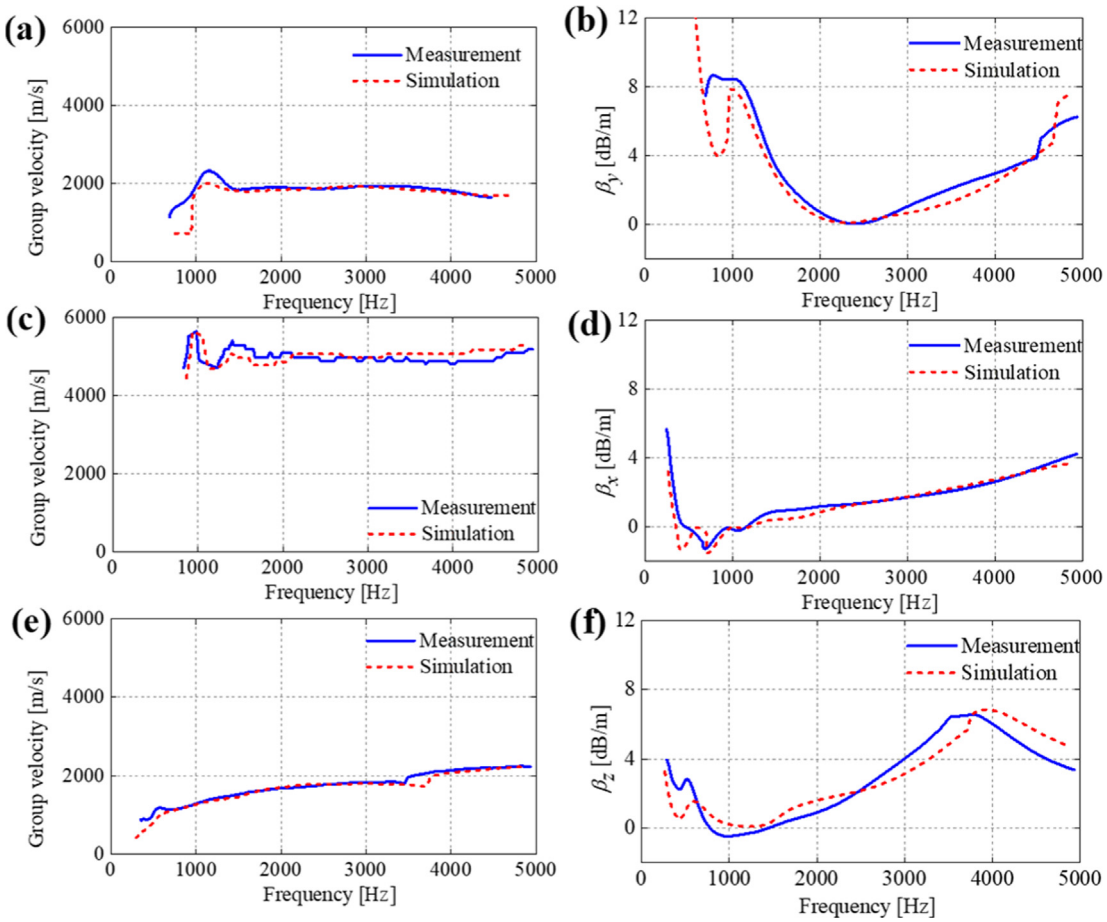

Fig. 18. Comparison of measured and simulated group velocities and attenuation coefficient. (a) Vertical group velocity; (b) vertical attenuation coefficient; (c) longitudinal group velocity; (d) longitudinal attenuation coefficient; (e) lateral group velocity; (b) lateral attenuation coefficient.

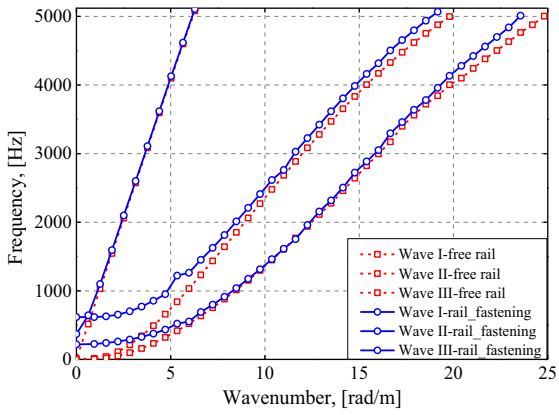

Fig. 19. Wavenumber-frequency dispersion curves of vertical bending waves (I), longitudinal compression waves (II), lateral bending waves (III) for rail-fastening with railpad Zw692-4 (—). Curves for free rail (---) as in [27].

Fig. 22 shows the influence of fastening damping on rail wave propagation characteristics in the three directions. The group velocities are almost identical with different fastening damping, as shown in Fig. 22a, c, e. The vertical and longitudinal attenuation coefficients go up overall with a damping increase in the whole frequency range. In the lateral direction, the attenuation coefficient below 1300 Hz and above 3100 Hz increases with larger damping.

Table 2
The simulation cases and their parameters.

Case	Vertical stiffness (MN/m)	Vertical damping (kNs/m)	Longitudinal stiffness (MN/m)	Longitudinal damping (kNs/m)	Lateral stiffness (MN/m)	Lateral damping (kNs/m)
0	600	16	160	6	160	20
1	300	16	160	6	160	20
2	1200	16	160	6	160	20
3	600	8	160	6	160	20
4	600	32	160	6	160	20
5	600	16	80	6	160	20
6	600	16	320	6	160	20
7	600	16	160	3	160	20
8	600	16	160	12	160	20
9	600	16	160	6	80	20
10	600	16	160	6	320	20
11	600	16	160	6	160	10
12	600	16	160	6	160	40

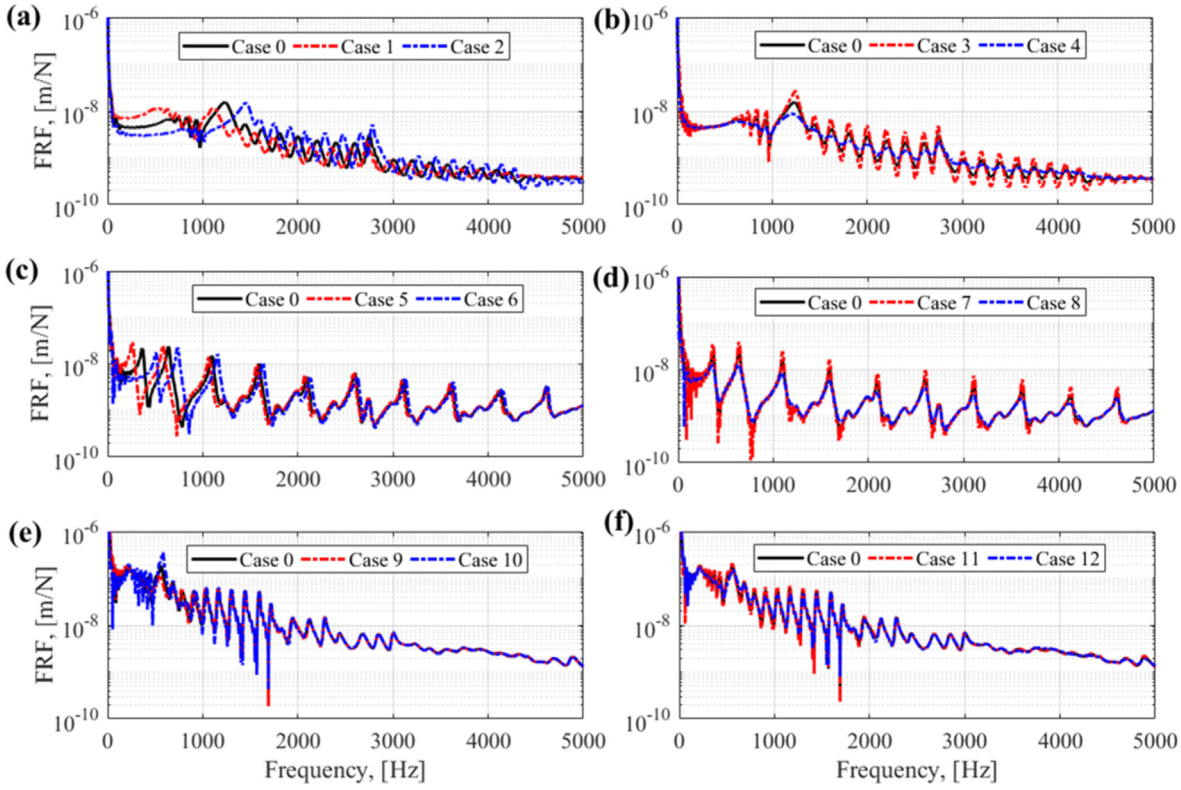

Fig. 20. The influences of fastening parameters on FRFs. (a) Vertical stiffness on vertical FRFs. (b) Vertical damping on vertical FRFs. (c) Longitudinal stiffness on longitudinal FRFs. (d) Longitudinal damping on longitudinal FRFs. (e) Lateral stiffness on lateral FRFs. (f) Lateral damping on lateral FRFs.

The results in Figs. 21 and 22 provide insights into the control of wave propagation for the mitigation of rolling noise. It was reported in [6] that the vertical and lateral waves of rail are dominant for rolling noise radiation in 500–1600 Hz. From Fig. 21b, we can see that increasing vertical stiffness can significantly increase the wave attenuation coefficient in this frequency range and thus mitigate rolling noise. The results in Fig. 22b and f indicate increase fastening damping could significantly increase the wave attenuation in a wide frequency range, which helps for rolling noise mitigation.

6. Discussions

An experimental setup consisting of rail-fastening was constructed in the laboratory to investigate the effect of fastening constraint on rail vibration modes and wave propagation. Compared to the field track, this setup used a short length of rail (4.97 m) and did not include the sleepers, ballasts, and other substructures. In this section, both in situ experiments and

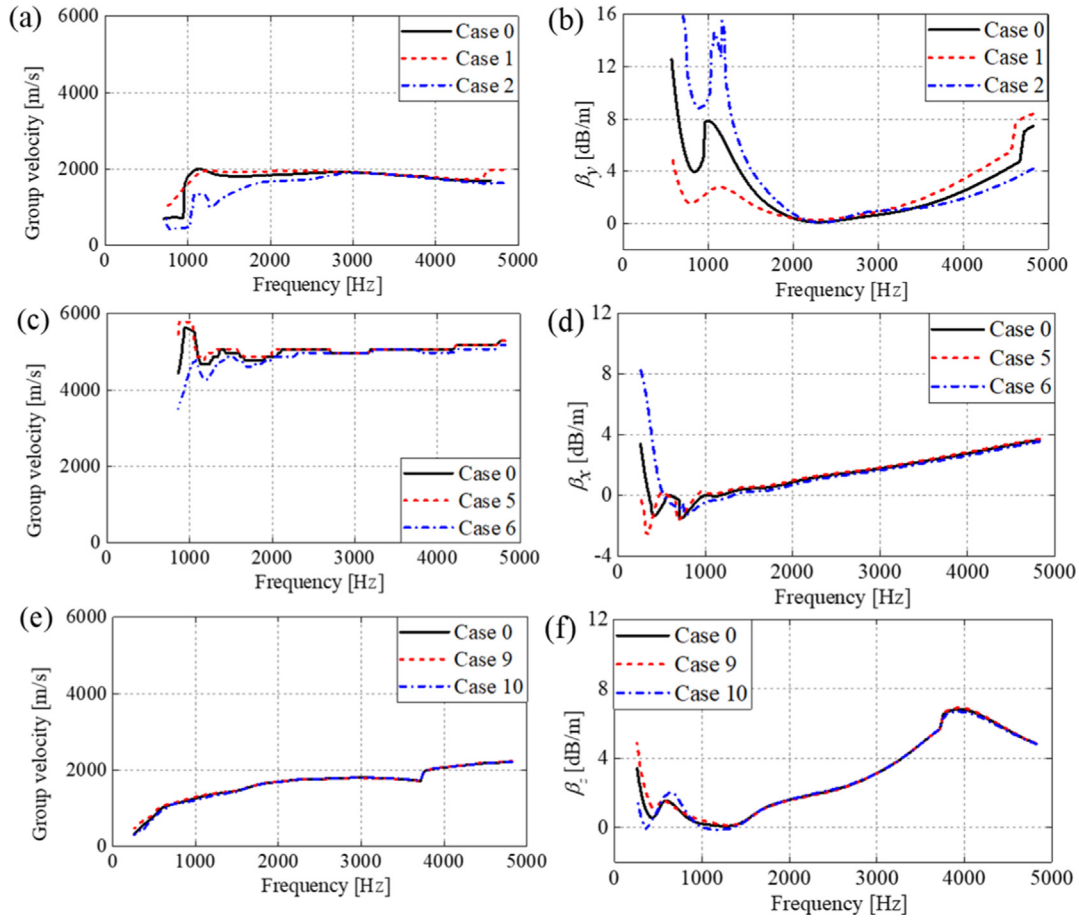

Fig. 21. The influences of fastening stiffness on wave propagation characteristics. (a) Vertical group velocity; (b) vertical attenuation coefficient; (c) longitudinal group velocity; (d) longitudinal attenuation coefficient (e) lateral group velocity; (f) lateral attenuation coefficient.

numerical simulations have been conducted to discuss the influence of these differences on rail vibration modes and wave propagation.

6.1. Field SMAW measurement of wave propagation characteristics

The wave propagation characteristics of the rail in field track were measured by the SMAW approach. The experimental setup is shown in Fig. 23. The track without visible defect is in Railway Testing center Faurei, Romania. The UIC60 E1 rail was constrained by Vossloh W14 fastenings on prestressed monoblock sleepers every 0.6 m. No joints, welds and crossings are nearby. The track can thus be considered as effectively infinite. Eleven 3D accelerometers (PCB 356B21, denoted as 1–11 in Fig. 23) were used to measure the rail vibrations under the impact of the hammer. Accelerometers 1–7 were glued onto the railhead on the field side. Among them, accelerometers 1 and 4 were above the sleeper (called on-support below); accelerometers 2 and 6 were at the mid-span of the rail; and accelerometers 3, 5 and 7 were at the quarter-span. Accelerometers 8 and 10 were glued onto the rail web, and accelerometers 9 and 11 were glued onto the rail foot. The tests in the longitudinal directions were not performed because of the difficulty in applying longitudinal excitation on the railhead.

The WPSs in Fig. 24a, b and c show the propagation and dispersion of vertical and lateral waves of the rail in the field track. Fig. 25 shows the measured group velocities and attenuation coefficients from the laboratory (see Section 3.2) and the field. Compared to the results in Section 3.2, reasonable agreements have been achieved between the laboratory and field measurements. For instance, the vertical group velocities at 1000–3500 Hz in these two cases fluctuate at approximately 2000 m/s and both have a downward trend above 3500 Hz. The lateral group velocities both have an overall upward trend and rise to over 2200 m/s at 4500 Hz. The vertical wave attenuation of field measurement is relatively low in 1200–3200 Hz, which shares a similar frequency range to that of laboratory measurement in 1800–3600 Hz. The lateral wave attenuation of field measurement also has a valley at about 600 Hz and a peak at approximately 3800 Hz, similar to that of laboratory measurement. These agreements indicate that the experimental setup of rail-fastening in the laboratory is appropriate to inves-

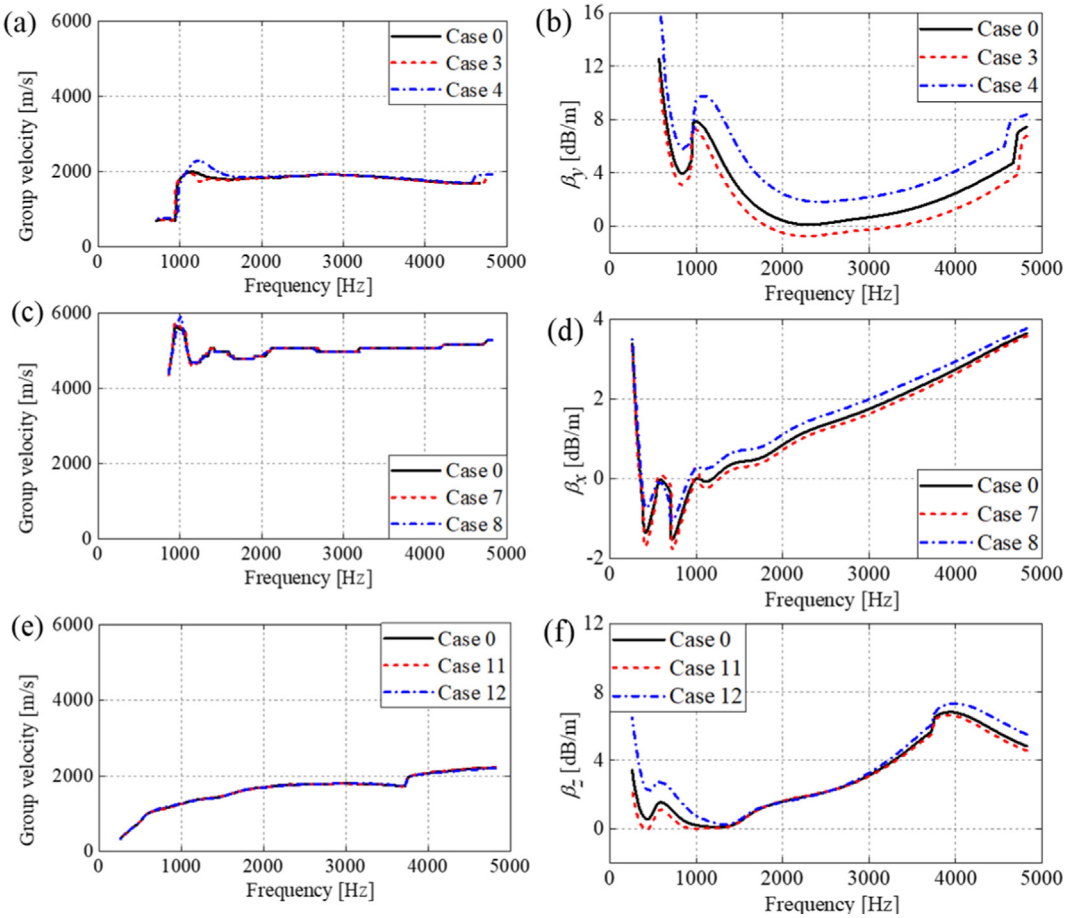

Fig. 22. The influences of fastening damping on wave propagation characteristics. (a) Vertical group velocity; (b) vertical attenuation coefficient; (c) longitudinal group velocity; (d) longitudinal attenuation coefficient (e) lateral group velocity; (f) lateral attenuation coefficient.

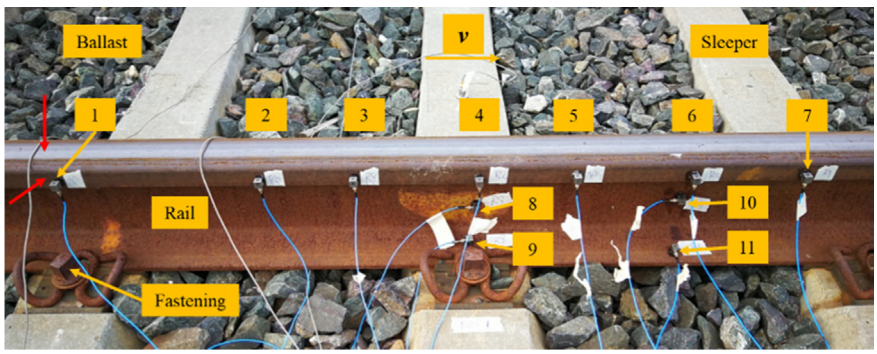

Fig. 23. Experimental setup of ODS and SMAW measurements in the field track. The red arrows indicate the vertical and lateral hammer excitation positions.

tigate wave propagation characteristics of the rail under fastening constraint, and the experimental results can be used to understand the vibrational rail waves in the field.

Some differences were also observed between the laboratory and field measurements. For example, the vertical group velocities of field measurement show strong fluctuation at lower frequencies; the values of the wave attenuation of field measurement are over three times larger than those of laboratory measurement at lower frequencies. In the field, the dynamic behaviors of the track can be characterized into three frequency range depending on the contribution of the track components [29,32,37,38,45]. In the low frequency range (0–40 Hz), the substructure layer mainly contributes to track

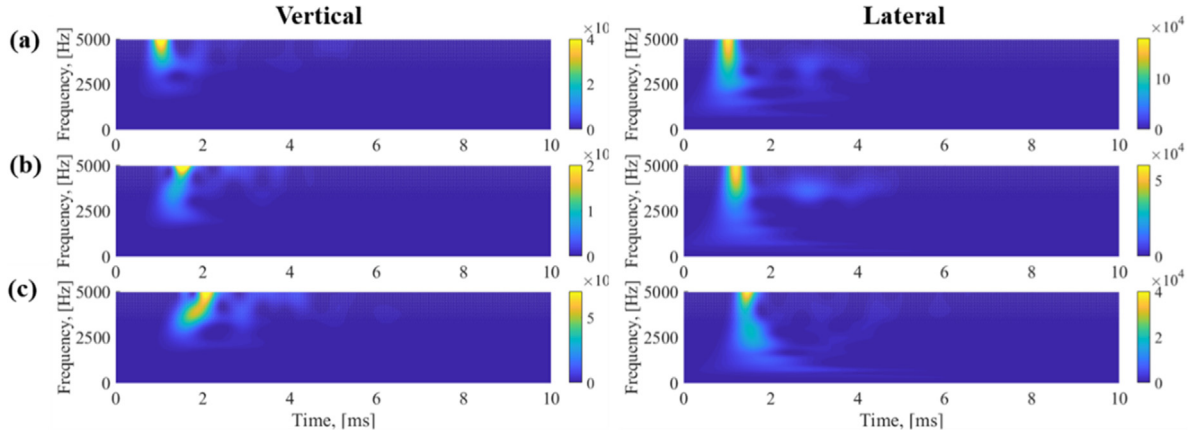

Fig. 24. Vertical and lateral WPSs at (a) accelerometer 1; (b) accelerometer 4; (c) accelerometer 7. The results of vertical WPSs are from [27].

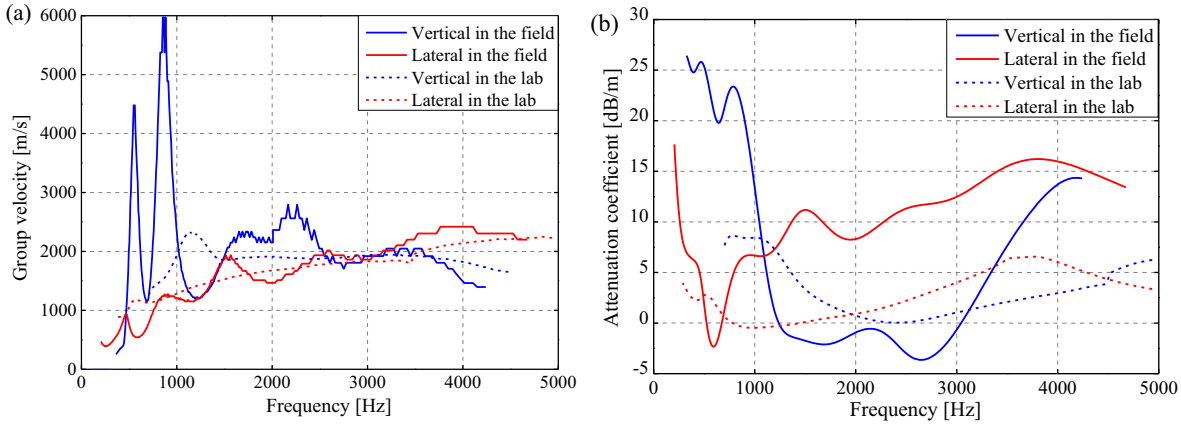

Fig. 25. Comparison of measured group velocities and attenuation coefficients of vertical and lateral waves from the laboratory and the filed. (a) Group velocities; (b) attenuation coefficient.

dynamic behaviors. In the mid frequency range (40–400 Hz), the sleeper (including sleeper pad) and ballast bed (concrete plates in ballastless track) are two key contributor to track dynamics. In the high frequency range (400–5000 Hz), the superstructure layer including sleeper, fastener and rail, provides the major contributions. Therefore, these differences between the laboratory and field measurements at lower frequencies range may be caused by the sleepers and ballast in the field track.

6.2. The influences of rail lengths on rail vibration modes

In the experimental setup (Fig. 2), a short length of rail (4.97 m) was used for the laboratory test, while in practice, it is normally much longer. Three simulation cases were designed to study the influence of the rail lengths on rail vibration modes, as shown in Fig. 26.

The simulated FRFs are shown in Fig. 27a, b and c. With the increase of the rail length, the number of peaks in the FRFs considerably increases, and the fluctuation amplitude of most peaks are reduced. That is because these peaks correspond to different types of rail vibration modes, e.g., longitudinal compression modes, vertical bending modes and lateral bending modes, respectively (as indicated by arrows in Fig. 27). With the increase of rail length, the number of rail vibration modes increases and their frequencies are also different in the same frequency range [27]. When the rail length is up to 20 m, the fluctuation amplitudes of the vertical and lateral FRFs are so small that the FRF curves become almost smooth. Nevertheless, the fluctuation amplitude of the longitudinal FRF is still relatively strong, indicating longer rail is needed to suppress the longitudinal compression modes.

In the field, the nominal rail length is long, and the track dynamics are closer to the vibration responses of the 20-m rail, as shown in Fig. 27d. Rail resonances and pinned-pined resonances are the dominant vibration modes [32,37,38]. In some conditions, rails may have welds and joints or defects like cracks, which cause energy reflections at these locations.

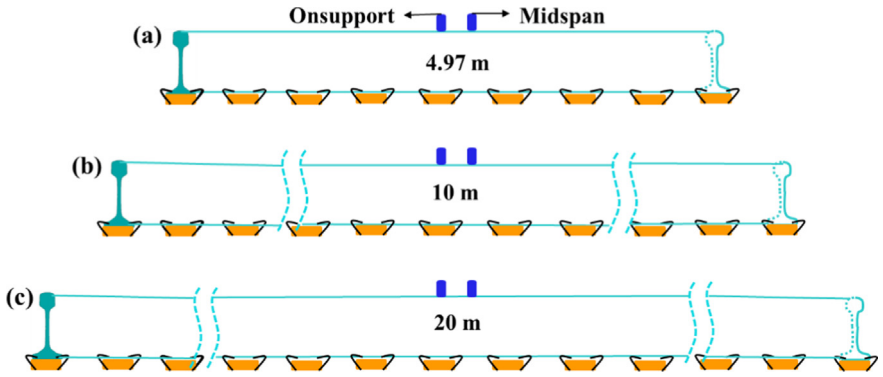

Fig. 26. Different rail lengths in the FE simulations. (a) 4.97 m; (b) 10 m; (c) 20 m.

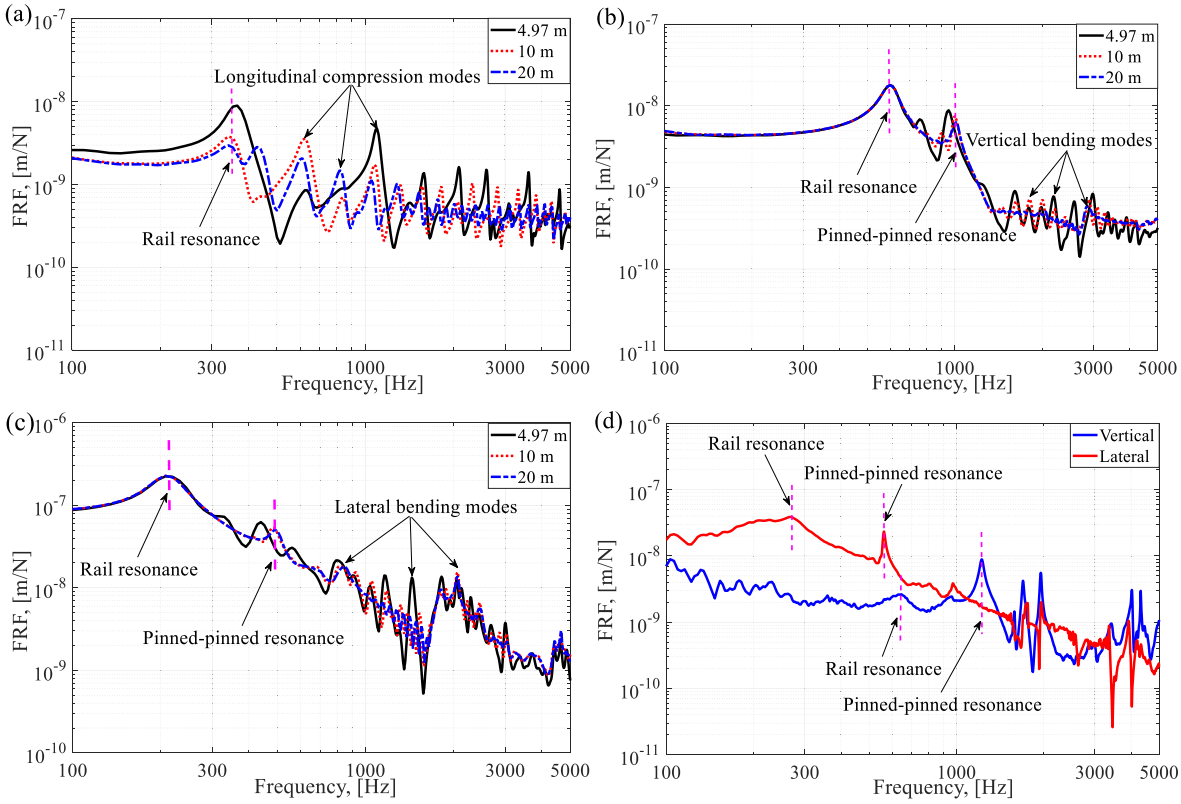

Fig. 27. Simulated FRFs at mid-span with different rail lengths and measured FRFs at mid-span. (a) Simulated longitudinal FRFs; (b) simulated vertical FRFs; (c) simulated lateral FRFs; (d) measured vertical and lateral FRFs.

7. Conclusions

This paper presents a systematic methodology to study rail vibration modes and wave propagation under fastening constraint in three directions up to 5000 Hz. This method includes three steps: 1) experimental investigation of rail vibrations under fastening constraint; 2) the validation and analysis of 3D FE modeling of rail-fastening; and 3) rail vibration control by fastening parameters. In Step 1, an experimental setup consisting of rail-fastening was constructed in the laboratory. Two types of railpads, the harder Zw692-4, and the softer FC9, were tested in this setup. ODS and SMAW measurements were conducted to identify rail vibration modes and measure wave propagation characteristics under fastening constraint. In Step 2, the 3D FE model of rail-fastening was developed and validated with the ODS and SMAW measurement results. The wavenumber-frequency dispersion curves of vibrational rail waves were derived from analyzing the experimental results.

In Step 3, insights into rail vibration control were gained through sensitivity analysis of fastening dynamic parameters. Finally, the measured rail vibrations under fastening constraint in the laboratory and field tests are compared, and reasonable agreement has been found. This agreement indicates that the experimental setup of rail-fastening in the laboratory is appropriate for investigating wave propagation characteristics of the rail under fastening constraint, and the experimental results can be used to understand the vibrational rail waves in the field. The main conclusions are summarized as follows.

Vertical bending modes, longitudinal compression modes, and lateral bending modes of the rail under fastening constraint are identified from the ODS measurement but with shifted frequencies and significantly reduced vibration amplitude compared to that of free rail. The lateral torsion modes, web 1st bending modes and web 2nd bending modes of rail-fastening are not identifiable, which are possibly suppressed by the fastening constraint.

Wave propagation characteristics in terms of group velocities and attenuation coefficients were measured from WPSs of rail-fastening by SMAW measurement. Fastening constraint considerably increases the wave attenuation along the rail in all three directions. One noticeable peak occurs at around 1150 Hz in the vertical group velocity of rail-fastening. The longitudinal group velocity almost does not change under fastening constraint at a value of around 5100 m/s. Vertical wave attenuation of rail-fastening is relatively small between 1800 and 3600 Hz. Lateral wave attenuation of rail-fastening shows a dominant peak at about 3800 Hz.

Compared to the vertical and lateral directions, the fastenings constrain the longitudinal rail vibrations less strongly, which could be seen from the following facts: (1) all the longitudinal compression modes are distinguishable in FRFs up to 5000 Hz while the vertical and lateral modes can only be observed in a narrower frequency band; (2) the fluctuation amplitude of the longitudinal modes is larger than those in the vertical and lateral directions; (3) the attenuation coefficient of a longitudinal wave is generally lower than those in the vertical and lateral directions.

The results of sensitivity analysis indicate that the change of fastening stiffness and damping can control rail mode frequencies and their vibration amplitude, and influence the wave propagation velocities and attenuation along the rail. Therefore, the optimization of fastening parameters could be helpful for mitigation of short pitch corrugation and wheel-rolling noise in the relevant frequency range, which needs further research in future work.

In summary, this work contributes to a better understanding of 3D rail vibrations under fastening constraint and provides insights into rail vibration control by fastening dynamic parameters. In future work, the optimization design of rail constraint will be performed to suppress rail vibrations better. More accelerometers should be mounted on the rail to obtain better spatial resolution and to more accurately identify the rail vibration modes at higher frequencies by ODS measurement. The fastening model could be improved by, e.g., a more complex Prony series model to consider the nonlinear properties of the railpads in order to further narrow the gap between measurements and simulations.

CRediT authorship contribution statement

Pan Zhang: Conceptualization, Methodology, Software, Formal analysis, Data curation, Investigation, Writing - original draft, Writing - review & editing, Visualization. **Shaoguang Li:** Validation, Investigation, Software, Writing - review & editing. **Alfredo Núñez:** Methodology, Writing - review & editing, Visualization, Supervision, Funding acquisition. **Zili Li:** Conceptualization, Methodology, Resources, Writing - review & editing, Supervision, Project administration, Funding acquisition.

Declaration of Competing Interest

The authors declare that they have no known competing financial interests or personal relationships that could have appeared to influence the work reported in this paper.

Acknowledgment

This work was partly supported by the China Scholarship Council.

References

[1] K. Hempelmann, K. Knothe, An extended linear model for the prediction of short pitch corrugation, Wear 191 (1–2) (1996) 161–169, https://doi.org/10.1016/0043-1648(95)06747-7.
[2] S.L. Grassie, Rail corrugation: characteristics, causes, and treatments, Proc. Inst. Mech. Eng. Part F: J. Rail Rapid Transit 223 (6) (2009) 581–596, https://doi.org/10.1243/09544097jrrt264.
[3] S. Li, Z. Li, A. Núñez, R. Dollevoet, New insights into the short pitch corrugation enigma based on 3D-FE coupled dynamic vehicle-track modeling of frictional rolling contact, Appl. Sci. 7(8) (2017). doi: 10.3390/app7080807.
[4] D.J. Thompson, Wheel-rail noise generation, Part III: rail vibration, J. Sound Vib. 161 (3) (1993) 421–446, https://doi.org/10.1006/jsvi.1993.1084.
[5] D.J. Thompson, B. Hemsworth, N. Vincent, Experimental validation of the twins prediction program for rolling noise, Part 1: description of the model and method, J. Sound Vib. 193 (1) (1996) 123–135, https://doi.org/10.1006/jsvi.1996.0252.
[6] D.J. Thompson, P. Fodiman, H. Mahé, Experimental validation of the twins prediction program for rolling noise, Part 2: results, J. Sound Vib. 193 (1) (1996) 137–147, https://doi.org/10.1006/jsvi.1996.0253.
[7] H. Ilias, The influence of railpad stiffness on wheelset/track interaction and corrugation growth, J. Sound Vib. 227 (5) (1999) 935–948, https://doi.org/10.1006/jsvi.1999.2059.
[8] Y. Shen, Z. Xing, S. Yang, J. Sun, Parameters optimization for a novel dynamic vibration absorber, Mech. Syst. Sig. Process. 133s (2019), https://doi.org/10.1016/j.ymssp.2019.106282.

[9] D. Thompson, C. Jones, T. Waters, D. Farrington, A tuned damping device for reducing noise from railway track, Appl. Acoust. 68 (1) (2007) 43–57.
[10] X. Wang, B.T. Yang, Transient vibration control using nonlinear convergence active vibration absorber for impulse excitation, Mech. Syst. Sig. Process. 117 (2019) 425–436, https://doi.org/10.1016/j.ymssp.2018.07.038.
[11] A. Johansson, J.C.O. Nielsen, R. Bolmsvik, A. Karlström, R. Lundén, Under sleeper pads—influence on dynamic train–track interaction, Wear 265 (9–10) (2008) 1479–1487, https://doi.org/10.1016/j.wear.2008.02.032.
[12] K. Wei, Q.L. Yang, Y.L. Dou, F. Wang, P. Wang, Experimental investigation into temperature- and frequency-dependent dynamic properties of high-speed rail pads, Constr. Build. Mater. 151 (2017) 848–858, https://doi.org/10.1016/j.conbuildmat.2017.06.044.
[13] A. Fenander, Frequency dependent stiffness and damping of railpads, P I Mech. Eng. F-J. Rai 211 (1) (1997) 51–62, https://doi.org/10.1243/0954409971530897.
[14] D.J. Thompson, Developments of the indirect method for measuring the high frequency dynamic stiffness of resilient elements, J. Sound Vib. 213 (1) (1998) 169–188, https://doi.org/10.1006/jsvi.1998.1492.
[15] J. Maes, H. Sol, P. Guillaume, Measurements of the dynamic railpad properties, J. Sound Vib. 293 (3–5) (2006) 557–565, https://doi.org/10.1016/j.jsv.2005.08.042.
[16] M. Oregui, A. de Man, M.F. Woldekidan, Z. Li, R. Dollevoet, Obtaining railpad properties via dynamic mechanical analysis, J. Sound Vib. 363 (2016) 460–472, https://doi.org/10.1016/j.jsv.2015.11.009.
[17] L.B. Eldred, W.P. Baker, A.N. Palazotto, Kelvin-Voigt versus fractional derivative model as constitutive relations for viscoelastic materials, AIAA J. 33 (3) (1995) 547–550, https://doi.org/10.2514/3.12471.
[18] B. Ripke, Hochfrequente Gleismodellierung und Simulation der Fahrzeug-Gleis-Dynamik unter Verwendung einer nichtlinearen Kontaktmechanik, 1995.
[19] A. Fenander, A fractional derivative railpad model included in a railway track model, J. Sound Vib. 212 (5) (1998) 889–903, https://doi.org/10.1006/jsvi.1997.1483.
[20] J. Xu, J. Li, Stochastic dynamic response and reliability assessment of controlled structures with fractional derivative model of viscoelastic dampers, Mech. Syst. Sig. Process. 72–73 (2016) 865–896, https://doi.org/10.1016/j.ymssp.2015.11.016.
[21] M. Oregui, Z. Li, R. Dollevoet, An investigation into the modeling of railway fastening, Int. J. Mech. Sci. 92 (Mar 2015) 1–11, https://doi.org/10.1016/j.ijmecsci.2014.11.019.
[22] J.I. Egana, J. Vinolas, M. Seco, Investigation of the influence of rail pad stiffness on rail corrugation on a transit system, Wear 261 (2) (2006) 216–224, https://doi.org/10.1016/j.wear.2005.10.004.
[23] D.J. Thompson, C.J.C. Jones, T.X. Wu, G. de France, The influence of the non-linear stiffness behaviour of rail pads on the track component of rolling noise, P I Mech. Eng. F-J. Rai 213 (4) (1999) 233–241, https://doi.org/10.1243/0954409991531173.
[24] K. Wei, F. Wang, P. Wang, Z.X. Liu, P. Zhang, Effect of temperature- and frequency-dependent dynamic properties of rail pads on high-speed vehicle-track coupled vibrations, Veh. Syst. Dyn. 55 (3) (Mar 2017) 351–370, https://doi.org/10.1080/00423114.2016.1267371.
[25] M. Oregui, A. Nunez, R. Dollevoet, Z.L. Li, Sensitivity analysis of railpad parameters on vertical railway track dynamics, J. Eng. Mech. 143(5) (May 2017). doi: Artn 0401701110.1061/(Asce)Em.1943-7889.0001207.
[26] Z. Yang, A. Boogaard, R. Chen, R. Dollevoet, Z.L. Li, Numerical and experimental study of wheel-rail impact vibration and noise generated at an insulated rail joint, Int. J. Impact Eng. 113 (Mar 2018) 29–39, https://doi.org/10.1016/j.ijimpeng.2017.11.008.
[27] P. Zhang, S. Li, A. Núñez, Z. Li, Multimodal dispersive waves in a free rail: numerical modeling and experimental investigation, Mech. Syst. Sig. Process. 150 (2021), https://doi.org/10.1016/j.ymssp.2020.107305.
[28] T. Hayashi, W.J. Song, J.L. Rose, Guided wave dispersion curves for a bar with an arbitrary cross-section, a rod and rail example, Ultrasonics 41 (3) (May 2003) 175–183, https://doi.org/10.1016/s0041-624x(03)00097-0.
[29] A. Man, Dynatrack: A survey of dynamic railway track properties and their quality, 2004.
[30] M. Oregui, Z. Li, R. Dollevoet, Identification of characteristic frequencies of damaged railway tracks using field hammer test measurements, Mech. Syst. Sig. Process. 54–55 (Mar 2015) 224–242, https://doi.org/10.1016/j.ymssp.2014.08.024.
[31] K. Giannakos, Modeling the influence of short wavelength defects in a railway track on the dynamic behavior of the Non-Suspended Masses, Mech. Syst. Sig. Process. 68–69 (Feb 2016) 68–83, https://doi.org/10.1016/j.ymssp.2015.07.020.
[32] S.L. Grassie, R.W. Gregory, D. Harrison, K.L. Johnson, The Dynamic-response of railway track to high-frequency vertical excitation, J. Mech. Eng. Sci. 24 (2) (1982) 77–90, https://doi.org/10.1243/Jmes_Jour_1982_024_016_02.
[33] L. Xu, W.M. Zhai, A three-dimensional model for train-track-bridge dynamic interactions with hypothesis of wheel-rail rigid contact, Mech. Syst. Sig. Process. 132 (2019) 471–489, https://doi.org/10.1016/j.ymssp.2019.04.025.
[34] R. Cettour-Janet, A. Barbarulo, F. Letourneaux, G. Puel, An Arnoldi reduction strategy applied to the semi-analytical finite element method to model railway track vibrations, Mech. Syst. Sig. Process. 116 (2019) 997–1016, https://doi.org/10.1016/j.ymssp.2018.07.013.
[35] I.I. Setshedi, P.W. Loveday, C.S. Long, D.N. Wilke, Estimation of rail properties using semi-analytical finite element models and guided wave ultrasound measurements, Ultrasonics 96 (Jul 2019) 240–252, https://doi.org/10.1016/j.ultras.2018.12.015.
[36] M. Oregui, Z.L. Li, R. Dollevoet, An investigation into the vertical dynamics of tracks with monoblock sleepers with a 3D finite-element model, P I Mech. Eng. F-J Rai 230 (3) (Mar 2016) 891–908, https://doi.org/10.1177/0954409715569558.
[37] S.L. Grassie, R.W. Gregory, K.L. Johnson, The dynamic-response of railway track to high-frequency lateral excitation, J. Mech. Eng. Sci. 24 (2) (1982) 91–95, https://doi.org/10.1243/Jmes_Jour_1982_024_017_02.
[38] S.L. Grassie, R.W. Gregory, K.L. Johnson, The dynamic-response of railway track to high-frequency longitudinal excitation, J. Mech. Eng. Sci. 24 (2) (1982) 97–102, https://doi.org/10.1243/Jmes_Jour_1982_024_018_02.
[39] N.M.M. Maia, J.M.M. e Silva, Theoretical and Experimental Modal Analysis, Research Studies Press, 1997.
[40] B.J. Schwarz, M.H. Richardson, Introduction to operating deflection shapes, CSI Reliability Week 10 (1999) 121–126.
[41] M. Vetterli, J. Kovacevic, Wavelets and subband coding (no. BOOK). Prentice-Hall, 1995.
[42] A. Grinsted, J.C. Moore, S. Jevrejeva, Application of the cross wavelet transform and wavelet coherence to geophysical time series, 2004.
[43] F.L. Di Scalea, J. McNamara, Measuring high-frequency wave propagation in railroad tracks by joint time-frequency analysis, J. Sound Vib. 273 (3) (2004) 637–651, https://doi.org/10.1016/S0022-460x(03)00563-7.
[44] W. Sachse, Y.H. Pao, On the determination of phase and group velocities of dispersive waves in solids, J. Appl. Phys. 49 (8) (1978) 4320–4327.
[45] C. Shen, R. Dollevoet, Z. Li, Fast and robust identification of railway track stiffness from simple field measurement, Mech. Syst. Sig. Process. 152 (2021), https://doi.org/10.1016/j.ymssp.2020.107431.